J. Fluid Mech. (2001), *vol.* 433, *pp.* 283–314. Printed in the United Kingdom

Dynamics of laser-induced cavitation bubbles near elastic boundaries: influence of the elastic modulus

By EMIL-ALEXANDRU BRUJAN†, KESTER NAHEN, PETER SCHMIDT AND ALFRED VOGEL‡

Medical Laser Center Lübeck, Peter-Monnik-Weg 4, D-23562 Lübeck, Germany

(Received 21 February 2000 and in revised form 23 October 2000)

The interaction of a laser-induced cavitation bubble with an elastic boundary is investigated experimentally by high-speed photography and acoustic measurements. The elastic material consists of a polyacrylamide (PAA) gel whose elastic properties can be controlled by modifying the water content of the sample. The elastic modulus, E, is varied between 0.017 MPa and 2.03 MPa, and the dimensionless bubble–boundary distance, γ, is for each value of E varied between $\gamma = 0$ and $\gamma = 2.2$. In this parameter space, jetting behaviour, jet velocity, bubble migration and bubble oscillation time are determined. The jetting behaviour varies between liquid jet formation towards or away from the elastic boundary, and formation of an annular jet which results in bubble splitting and the subsequent formation of two very fast axial liquid jets flowing in opposite directions. The liquid jet directed away from the boundary reaches a maximum velocity between $300\,\mathrm{m\,s^{-1}}$ and $600\,\mathrm{m\,s^{-1}}$ (depending on the elastic modulus of the sample) while the peak velocity of the jet directed towards the boundary ranges between $400\,\mathrm{m\,s^{-1}}$ and $800\,\mathrm{m\,s^{-1}}$ (velocity values averaged over $1\,\mu\mathrm{s}$). Penetration of the elastic boundary by the liquid jet is observed for PAA samples with an intermediate elastic modulus between 0.12 and 0.4 MPa. In this same range of elastic moduli and for small γ-values, PAA material is ejected into the surrounding liquid due to the elastic rebound of the sample surface that was deformed during bubble expansion and forms a PAA jet upon rebound. For stiffer boundaries, the bubble behaviour is mainly characterized by the formation of an axial liquid jet and bubble migration directed towards the boundary, as if the bubble were adjacent to a rigid wall. For softer samples, the bubble behaviour becomes similar to that in a liquid with infinite extent. During bubble collapse, however, material is torn off the PAA sample when bubbles are produced close to the boundary. We conclude that liquid jet penetration into the boundary, jet-like ejection of boundary material, and tensile-stress-induced deformations of the boundary during bubble collapse are the major mechanisms responsible for cavitation erosion and for cavitation-enhanced ablation of elastic materials as, for example, biological tissues.

† Present address: Department of Hydraulics, University Politechnica, Spl. Independentei 313, 77206 Bucharest, Romania: e-mail brujan@chmh.hydrop.pub.ro

‡ Author to whom correspondence should be addressed: e-mail vogel@mll.mu-luebeck.de

1. Introduction

In the preceding paper (Brujan *et al.* 2001, hereinafter referred to as Part 1) we investigated the interaction of a laser-induced cavitation bubble with an elastic polyacrylamide (PAA) sample as a function of the dimensionless stand-off parameter γ defined as the distance s between laser focus and boundary scaled by the maximum bubble radius R_{max}. The sample had an elastic modulus of 0.25 MPa and served as a transparent phantom for biological tissue. The interaction of the bubble with the elastic material was found to be very complex. At large values of the dimensionless distance ($\gamma \geqslant 0.9$), we observed an axial jet flow directed away from the boundary. For smaller γ-values, an annular jet was formed which led to bubble splitting and the formation of two very fast axial jets flowing in opposite directions. The maximum jet velocity towards the elastic boundary was determined to be 960 m s^{-1} (averaged over a time interval of 700 ns), and the jet could easily penetrate the boundary. For γ-values below 0.52, the elastic rebound of the PAA surface after deformation by the expanding cavitation bubble resulted in the formation of a PAA jet ejecting material into the liquid. Both liquid jet penetration into the sample and material ejection into the liquid increase the mass removal produced by pulsed laser ablation far beyond the amount of material which can be evaporated by the laser pulse.

In Part 1 we focused attention on a specific case where the elastic behaviour of the boundary has a particularly strong influence on the bubble dynamics, and we varied the distance between bubble and boundary to study the general principles of the bubble–boundary interaction. In the present study, the investigations are extended to a much larger part of the (E, γ)-parameter space, and the results are interpreted using the insight into fundamental mechanisms gained in Part 1.

The elastic properties of the PAA gel can be controlled by modifying its water content. The elastic modulus is varied between 0.017 MPa and 2.03 MPa. This range covers the elastic properties of various biological tissues, such as renal parenchyma (0.06 MPa) (Kodama & Tomita 2000), abdominal aorta (0.98–1.42 MPa), femoral artery (1.23–5.5 MPa), articular cartilage (0.43–1.15 MPa), muscle (0.06–0.8 MPa) (Duck 1990), and cornea (0.3–5 MPa) (Hoeltzel *et al.* 1992). For comparison, the bubble dynamics near a rigid aluminium sample is also investigated. With very small values of the elastic modulus, the boundary conditions approach the limit of an infinite fluid, and with increasing E-value, they resemble the case of a rigid boundary.

Our goal here is to present a complete overview of the jetting behaviour and boundary dynamics in the investigated part of the (E, γ)-space as well as quantitative information on the migration of the bubble centre and the maximum velocity of the liquid jets directed away from and towards the boundary. In addition, liquid jet penetration into the PAA sample and material ejection into the liquid are investigated. The results are, as in Part 1, discussed with respect to cavitation erosion, to collateral damage in laser surgery, and to cavitation-mediated enhancement of pulsed laser ablation and cutting of tissue.

2. Methods

2.1. *PAA samples*

The elastic boundary consisted of transparent gels of polyacryalmide (PAA) with a water content of 95%, 85%, 80%, 70%, 60% and 50%, respectively. For 70% water content, 60 g acrylamid and 1.6 g bis-acrylamide were mixed with 140 g of 0.22 M aqueous Tris buffer (pH 9.5) and 1 ml 10% amoniumpersulphate (APS). The

Sample	Water	PAA–95% water	PAA–85% water	PAA–80% water	PAA–70% water	PAA–60% water	PAA–50% water
E(MPa)	—	0.017 $\pm$0.0010	0.124 $\pm$0.004	0.252 $\pm$0.01	0.405 $\pm$0.01	1.04 $\pm$0.02	2.03 $\pm$0.15
ρ(kg m^{-3})	998	1012 ± 10	1032 ± 10	1050 ± 10	1073 ± 10	1095 ± 10	1123 ± 10
c_0(m s^{-1})	1483	1518 ± 15	1560 ± 15	1575 ± 15	1605 ± 15	1623 ± 15	1634 ± 15

TABLE 1. Values of elastic modulus, density and sound velocity of the PAA samples at 20 °C and ambient pressure.

solution was then placed in a plastic container and mixed with 0.2 ml N,N,N′,N′-tetramethylethylenediamine (TEMED) to initiate polymerization. For higher water content, the stock solution was diluted with buffer. For lower water content, a 50% stock solution was prepared and only 0.5 ml of APS and 50 µl TEMED were added to initiate polymerization. All components for the PAA-preparation were obtained from BioRad Laboratories. The thickness of each PAA sample was 20 mm and the area of the surface exposed to the cavitation bubble was $15 \times 15\,\mathrm{mm}^2$. The sample was mounted in a Teflon holder and completely immersed in water during experiments. PAA samples with low water content tend to take up water relatively fast. Experiments using PAA samples with 60% and 50% water content were, therefore, performed very quickly, within less than 1 minute after submersion of the samples into water, to avoid changes of the mechanical properties. Furthermore, in order to avoid any perturbations of the bubble dynamics caused by remnant deformations of the boundary, a new PAA sample was used for every laser exposure.

The elastic properties of the PAA samples were quantified by determining the stress–strain relation and calculating the elastic modulus, E, as the slope of the stress–strain curve. Uniaxial compression tests were performed on three specimens of PAA samples at each water content. The specimens were strained at a rate of $\dot{\varepsilon} = 1.7 \times 10^{-3}\,\mathrm{s}^{-1}$ using a universal testing machine (Zwick 1456). The elastic modulus of the PAA samples was determined at 10% strain, with a standard deviation in E smaller than 7%. The measured values of the elastic modulus, density and sound velocity of the PAA samples as a function of water content are given in table 1.

2.2. *Bubble generation and high-speed photography*

Cavitation bubbles were produced by focusing Nd:YAG laser pulses (Continuum YG 671-10) with 1064 nm wavelength and 6 ns duration into a glass cuvette filled with doubly distilled water. We used a constant pulse energy of 8 mJ $\pm$ 3% to produce bubbles with a constant maximum radius of $R_{\max} = 1.55 \pm 0.05$ mm. The methods employed for the determination of the bubble size are described in Part 1. We assumed that the maximum bubble volume does not change with variation of γ. For $\gamma < 1$ where the expanded bubble is non-spherical, $R_{\max}$ represents the radius of a spherical bubble with the same volume (equivalent spherical radius).

The bubble dynamics was recorded with a high-speed image converter camera (Hadland Photonics, Imacon 792) with framing rates up to 5 million frames s^{-1} and stored with a slow-scan CCD camera (Photometrics AT200A). The timing of the photography was adjusted with an electronic delay circuit. A schematic diagram depicting the experimental arrangement as well as a detailed description of the methods used are given in Part 1.

(*a*)

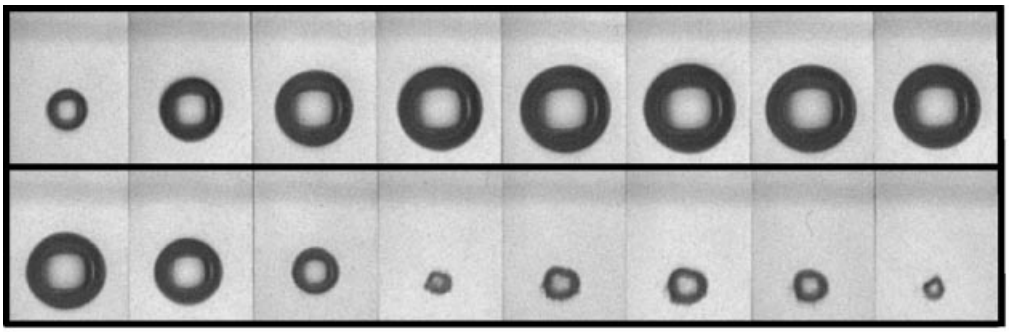

(*b*)

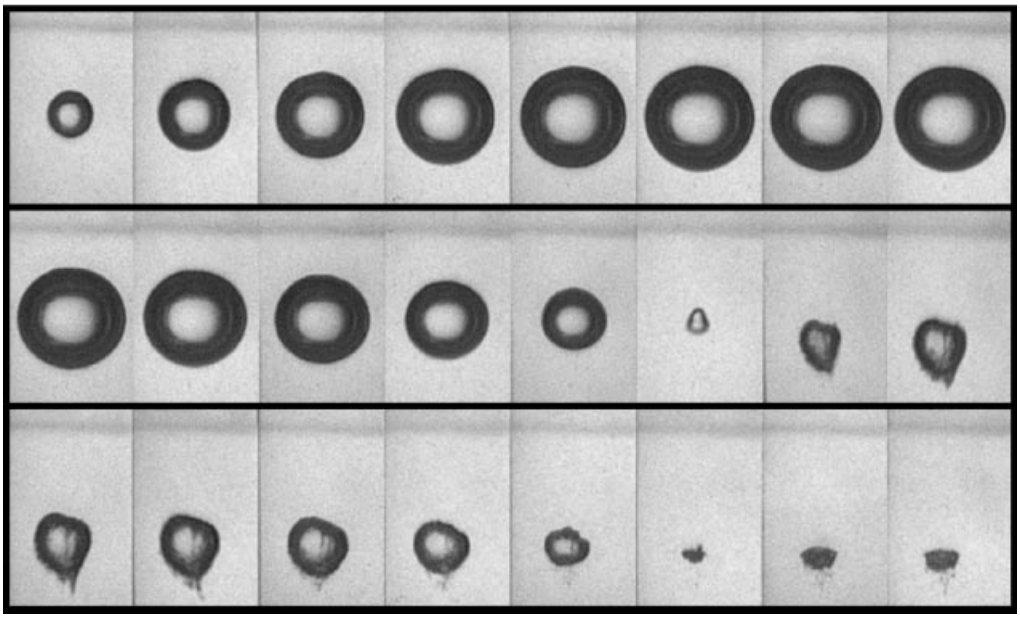

FIGURE 1 (*a,b*) For caption see facing page.

2.3. *Bubble oscillation times*

The oscillation time T_{osc} of a spherical bubble situated in a liquid of infinite extent is related to its maximum radius by (Rayleigh 1917)

$$T_{\mathrm{osc}} = 1.83 \left(\frac{\rho}{p - p_v} \right)^{1/2} R_{\mathrm{max}} \tag{2.1}$$

where ρ is the density of the liquid, p the static pressure and p_v the vapour pressure of the liquid. A boundary located close to the bubble leads, however, to a modification of its oscillation time depending on the non-dimensional stand-off parameter γ, so that (2.1) no longer holds. The modification (lengthening or shortening) factor k plotted against Rayleigh's oscillation time yields interesting information about the bubble–boundary interaction. The k-factor was, therefore, determined by measuring the oscillation time of bubbles of constant size ($R_{\mathrm{max}} = 1.55\,\mathrm{mm}$) as a function of

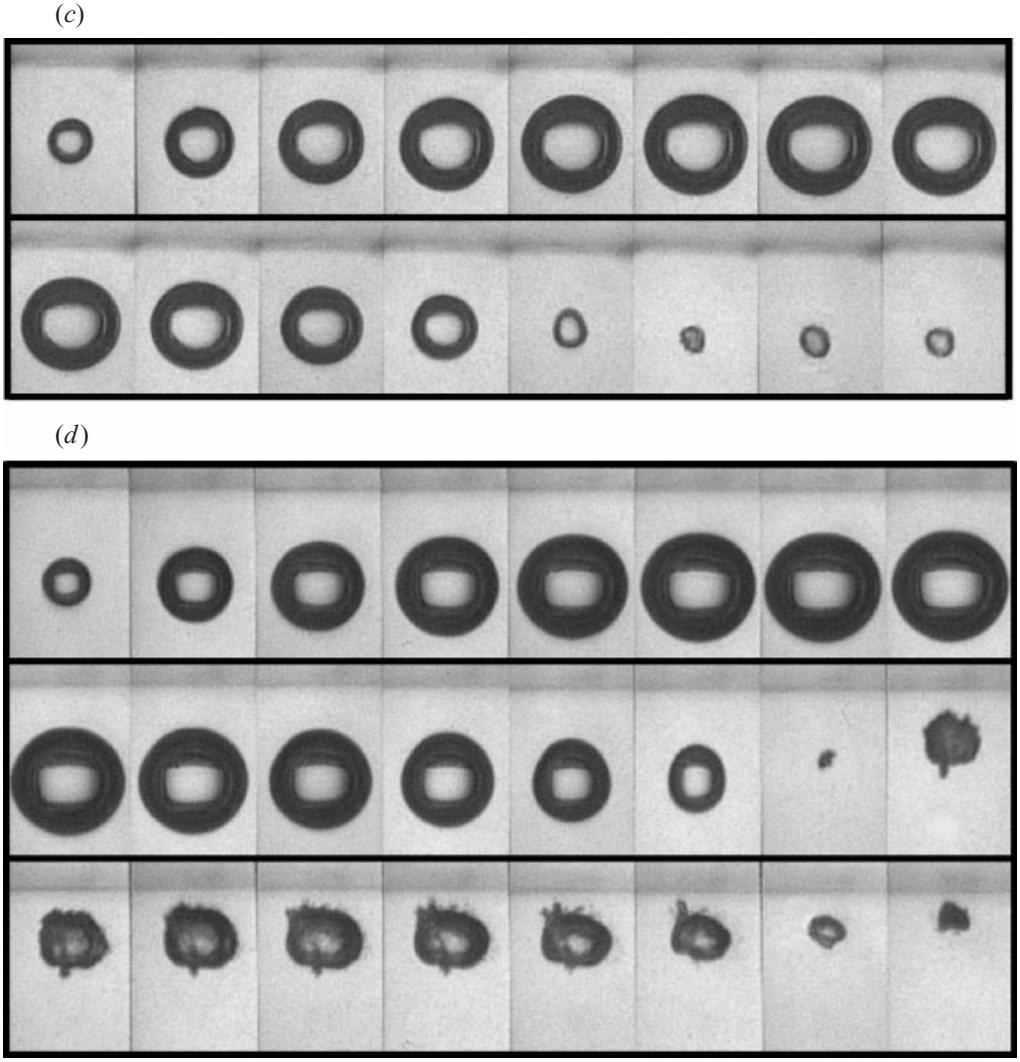

FIGURE 1. Growth and collapse of a laser-induced bubble near PAA samples with different water content c for $\gamma \approx 1.56$. (*a*) $c = 95\%$, $\gamma = 1.62$; (*b*) $c = 80\%$, $\gamma = 1.57$; (*c*) $c = 60\%$, $\gamma = 1.5$ and (*d*) $c = 50\%$, $\gamma = 1.58$. Frame interval 20 µs; frame width 3.5 mm.

γ. The oscillation period was obtained by measuring the time interval between the shock waves emitted during optical breakdown and bubble collapse using a fast PVDF hydrophone (Ceram, rise time 12 ns). The reference time for spherical bubble oscillation was determined at $\gamma > 10$.

Besides giving information about the bubble boundary interaction, the $k(\gamma)$ data enable R_{max} to be determined from the bubble oscillation time and the distance s between laser focus and boundary. In a first step, approximate values R_{max1} and γ_1 are calculated from the experimental data using (2.1). Correction of the measured value T_{osc} by the factor $k(\gamma_1)$ yields the more precise values R_{max2} and γ_2; correction of T_{osc} by $k(\gamma_2)$ yields R_{max3} and so on, until the required precision is reached.

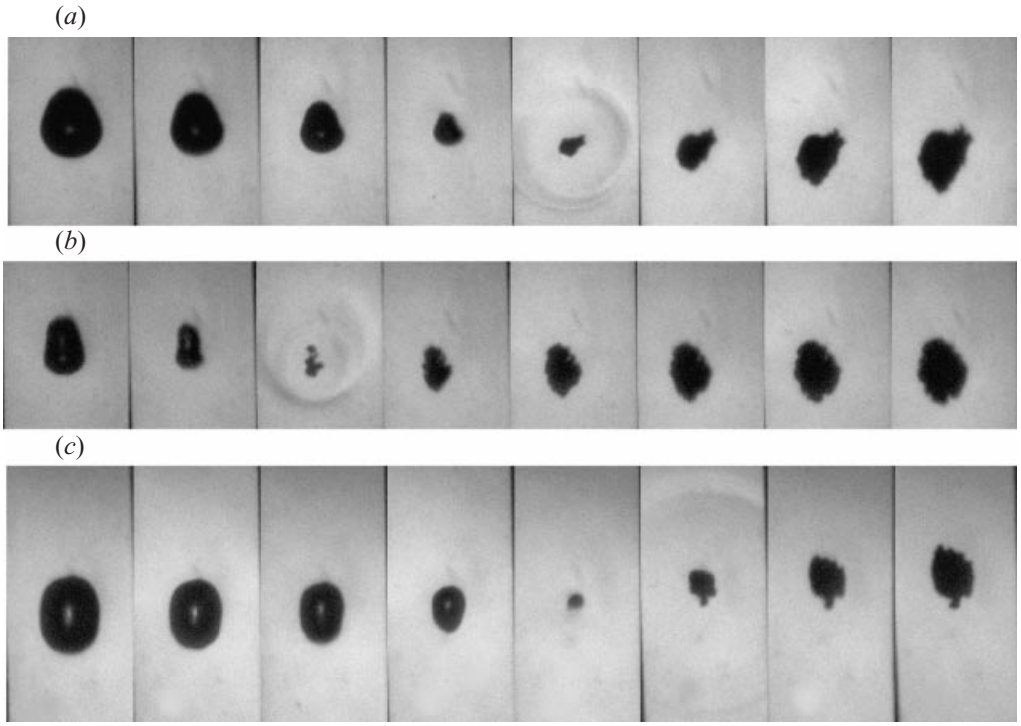

FIGURE 2. Collapse phase of a bubble near PAA samples with different water content c for $\gamma \approx 1.56$. (*a*) $c = 80\%$, $\gamma = 1.58$; (*b*) $c = 60\%$, $\gamma = 1.5$; (*c*) $c = 50\%$, $\gamma = 1.58$. Frame interval 1 μs; frame width 1.4 mm.

3. Results

3.1. *Bubble–boundary interaction and jetting behaviour*

Figures 1–9 show, for approximately constant γ-values, the interaction of a laser-induced cavitation bubble with an elastic boundary and the jetting behaviour at different values of the elastic modulus (corresponding to different water contents of the PAA samples). An overview of the dynamics in each case is presented using photography at 50 000 frames s^{-1} with diffuse illumination to visualize the jet inside the bubble. A more detailed view of the collapse phase is shown using 1 million frames s^{-1} and parallel illumination to visualize the shock wave emission upon bubble collapse and the deformation of the boundary. In all photographic series the elastic boundary is located in the upper part of the frames. We do not always show photographic series for all values of the elastic modulus, but illustrate mainly the changes of the jetting behaviour with varying material properties. A complete overview of the jetting behaviour is given in the schematic representation of figure 10. In this and all following high-speed photographic series, the maximum bubble radius is $R_{max} = 1.55 \pm 0.05$ mm.

3.1.1. *Material dependence of the dynamics for* $\gamma \approx 1.6$

Figures 1 and 2 show the bubble dynamics at a relatively large distance from the boundary (on average $\gamma = 1.56$). At 95% water content of the PAA sample (figure 1*a*), the bubble migrates slowly away from the boundary, but no jet is formed. The

influence of the boundary is too weak to induce jet formation because of the very small elastic modulus (large compliance) of the PAA sample.

At 80% water content of the PAA sample, the bubble achieves a cone-like shape during the last stage of the collapse. As a result, the collapse of the bubble wall facing the boundary is faster, leading to the formation of a liquid jet directed away from the boundary. This jet hits the opposite bubble wall, causing a funnel-shaped protrusion (figure 1*b*, frames 15–18 and figure 2*a*, frames 6–8).

When the bubble oscillates near the PAA sample with 60% water content (figures 1*c* and 2*b*), it migrates away from the boundary, but again no jet develops. The reason for this behaviour, however, differs from the reason for the similar dynamics at 95% water content where the influence of the elastic boundary was very weak. Here the repulsion due to the elastic rebound of the boundary is stronger, but it is balanced by the attractive Bjerknes force from the boundary. The magnitude of both forces is, however, too small to induce a pronounced flattening of the bubble into an oblate spheroid which would lead to the formation of an annular jet (see Part 1). The horizontal axis of the expanded bubble is only about 10% longer than the vertical axis (figure 1*c*, frame 6), and because of this small deviation from sphericity the liquid is preferentially drawn in from the sides only in a very late stage of bubble collapse where the bubble becomes elongated along the axis of symmetry (figure 2*b*, frames 1 and 2).

When the water content of the PAA sample is 50% (figures 1*d* and 2*c*), the bubble dynamics are similar to that near a rigid boundary (Vogel, Lauterborn & Timm 1989; Philip & Lauterborn 1998). During collapse, the bubble becomes elongated in a direction perpendicular to the boundary, it migrates towards the boundary, and a liquid jet directed towards the boundary is developed which leads to the protrusion of the bubble wall facing the boundary. The liquid jet is visible in the rebound phase as a dark line inside the bright central spot of the bubble.

3.1.2. *Material dependence of the dynamics for* $\gamma \approx 0.9$

Figures 3 and 4 show the dynamics for $\gamma \approx 0.88$, a value where the influence of the elastic boundary is already fairly strong. When the bubble oscillates near the PAA samples with 95% (figure 4*a*) and 85% water content (figures 3*a* and 4*b*), the formation of a high-speed liquid jet and bubble migration directed away from the boundary are the main features of the bubble dynamics. A mushroom-like shape of the bubble develops during the final stage of the collapse near the PAA sample with 85% water content (figure 3*a*, frame 13 and figure 4*b*, frames 1–3). The foot of the mushroom-shaped bubble collapses first, leading to the formation of the liquid jet directed away from the boundary.

For the PAA sample with 70% water content (figures 3*b* and 4*c*), the annular flow component is strong enough to induce bubble splitting. The splitting process is preceded by the formation of a mushroom-like shape of the bubble which develops very early during the collapse phase. The 'neck' of the mushroom-shaped bubble and the cavity situated farthest from the boundary collapse almost synchronously, emitting a pressure wave (figure 4*c*, frame 3) which accelerates the collapse of the cavity closer to the boundary. The result of the pressure wave impact on the upstream wall of the cavity is the formation of a high-speed liquid jet directed towards the boundary. The maximum velocity of this jet, averaged over the interframing time of 1 μs, is 680 m s^{-1}. The jet penetrates the PAA sample (figure 3*b*, frames 14–24) even though the distance between bubble and boundary is about 0.6 mm. This is the largest distance for which penetration of the PAA sample was observed. The maximum penetration depth of

(*a*)

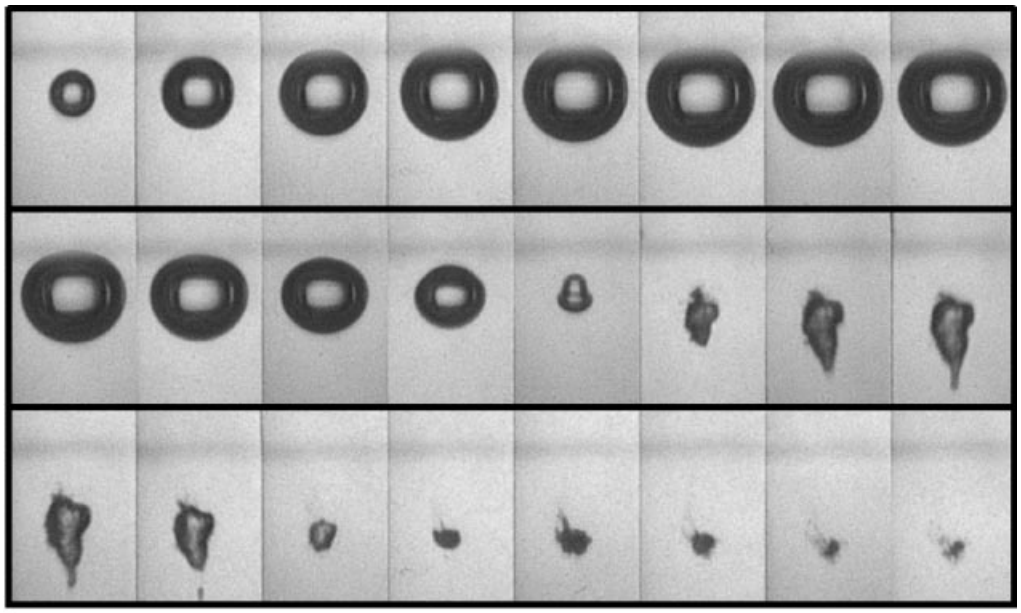

(*b*)

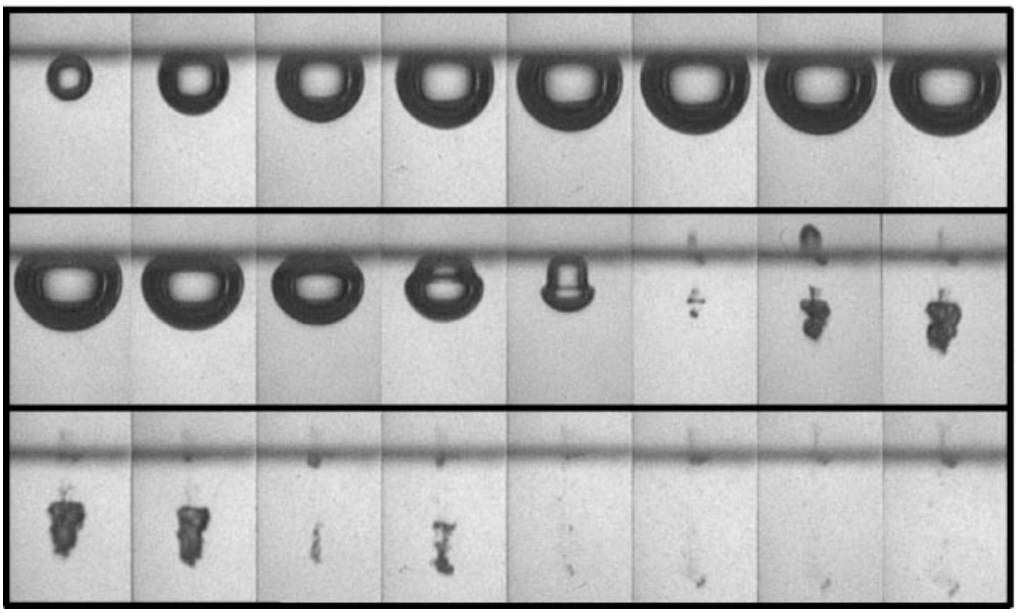

FIGURE 3 (*a,b*) For caption see facing page.

the liquid jet into the boundary, measured with respect to the undisturbed surface of the boundary, is about 0.7 mm.

For the PAA sample with 60% water content (figures 3*c* and 4*d*), the annular flow leading to bubble splitting and the formation of two high-speed liquid jets flowing in opposite directions again develops. However, the liquid jet does not penetrate into the PAA sample, because the plastic flow stress of the PAA material is now larger than the impact pressure caused by the jet.

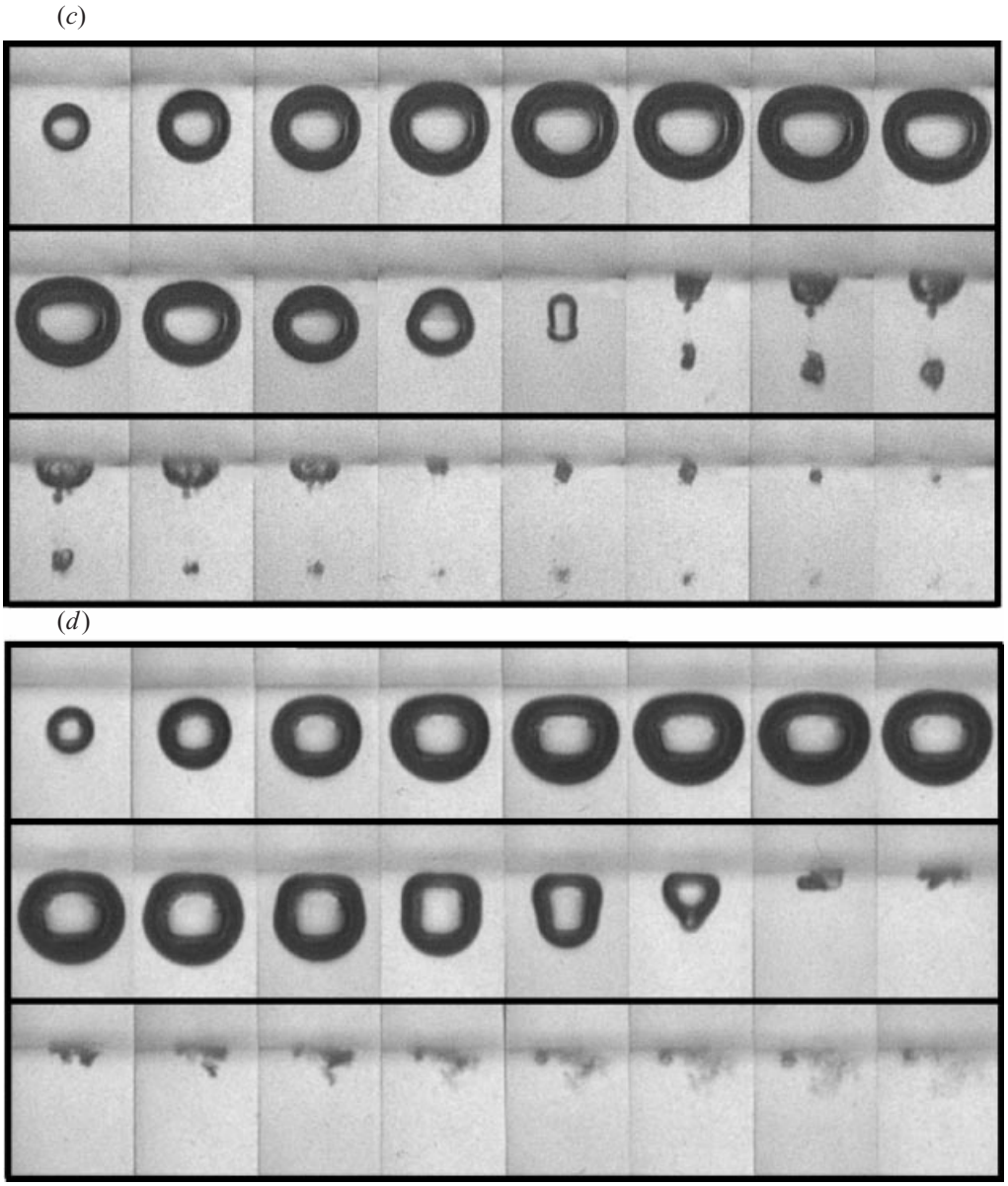

FIGURE 3. Growth and collapse of a laser-induced bubble near PAA samples with different water content c for $\gamma \approx 0.88$. (*a*) $c = 85\%$, $\gamma = 0.87$; (*b*) $c = 70\%$, $\gamma = 0.83$; (*c*) $c = 60\%$, $\gamma = 0.88$ and (*d*) $c = 50\%$, $\gamma = 0.87$. Frame interval 20 µs; frame width 3.5 mm.

For a PAA sample with 50% water content (figure 3*d* and 4*e*), no bubble splitting occurs and only a jet directed towards the boundary is formed. The asymmetric annular flow is, however, still manifested as a constriction of the polar region of the bubble on the side far from the elastic boundary. The constriction moves towards the pole and disappears during the final collapse stage. A similar development of the bubble shape during collapse is observed when the bubble collapses near an oscillating flat rigid wall (Blake *et al.* 1999) – most likely because the oscillation of the rigid wall resembles the sequence of indentation and rebound of the elastic boundary

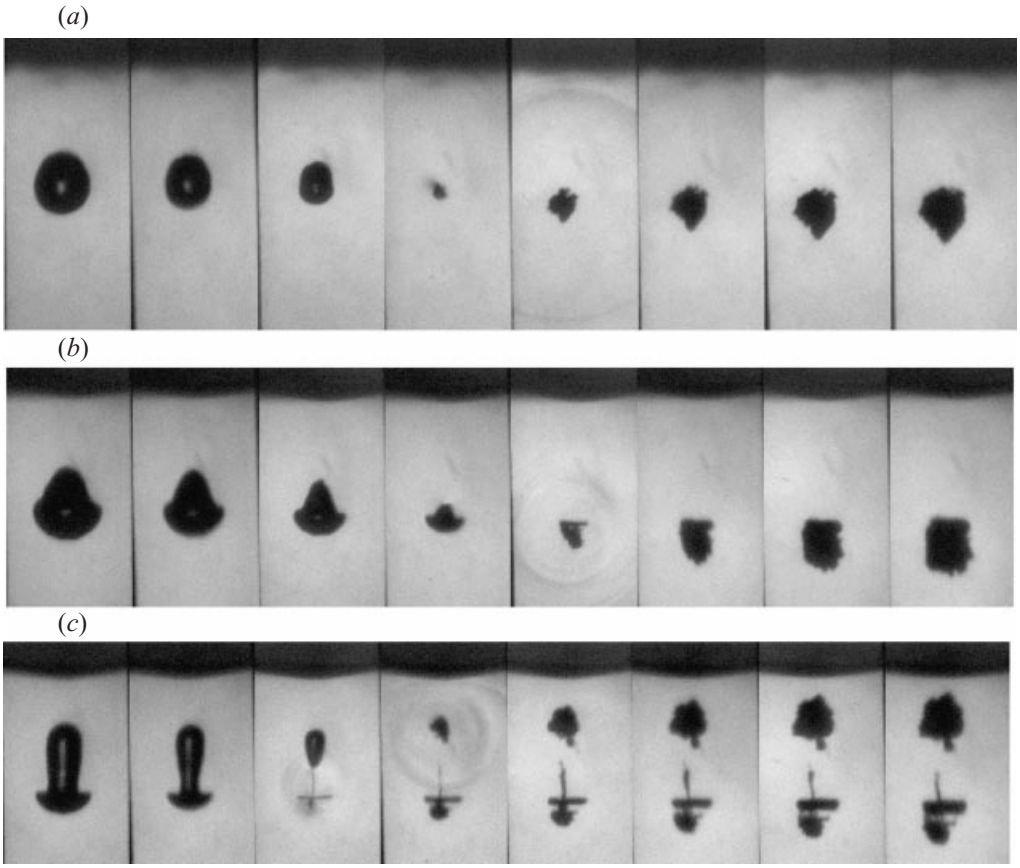

FIGURE 4 (*a,b*) For caption see facing page.

in the present study. The amplitude of the boundary deformation is certainly not large for samples with 50% water content, but some deformation must be assumed to explain the bubble dynamics observed. As in the case of 60% water content, no liquid jet penetration is observed because of the relatively high stiffness of the PAA material ($E = 2.03$ MPa) which is probably coupled with a high material strength. Another consequence of the high stiffness is that the boundary is hardly deformed by the tensile stress exerted during bubble collapse, unlike the cases of PAA samples with 85% to 60% water content.

The photographic series presented in figures 3 and 4 for $\gamma \approx 0.88$ illustrate how an increase in the sample elastic modulus results in an inversion of the direction of jet formation by changing the relative strength of the flows induced by the rebounding boundary and the Bjerknes attractive force. For small E-values, the flow induced by the rebounding surface dominates and the jet is directed away from the boundary. As the stiffness of the material increases, the Bjerknes attraction force becomes stronger. For the largest E-value, where the boundary is only slightly deformed, it becomes dominant and the jet is directed towards the boundary. At intermediate E-values (corresponding to 70% water content), the flow induced by the rebounding boundary and the Bjerknes force are approximately equal in strength. Therefore, the bubble achieves an oblate shape in the early collapse phase and collapses faster from the sides in a later stage. This leads to the formation of an annular jet which finally

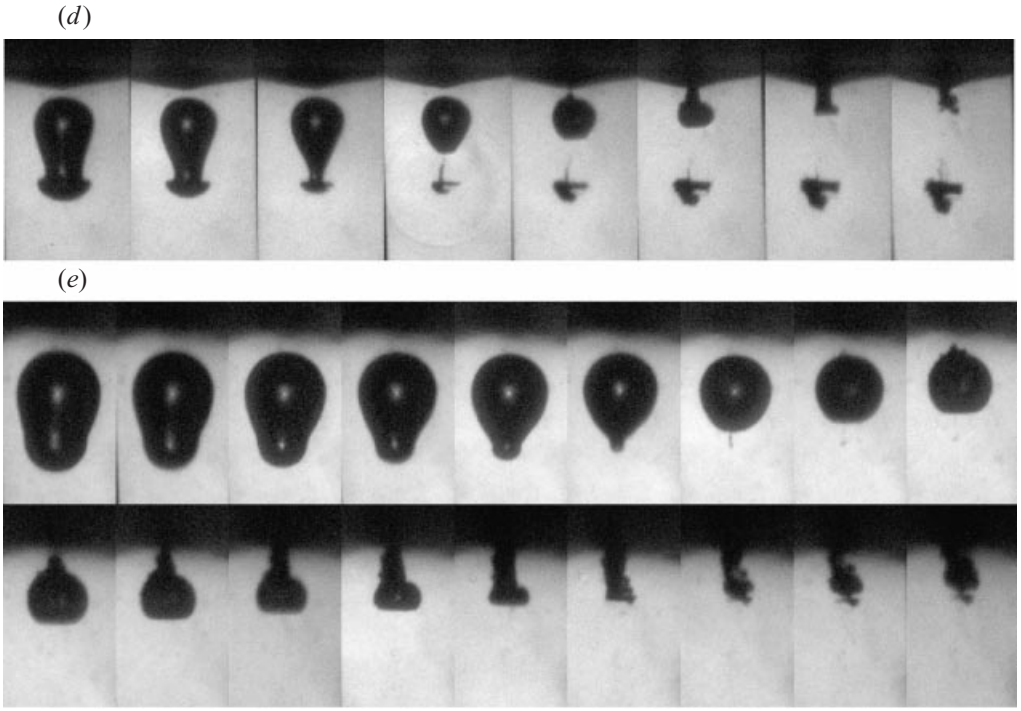

FIGURE 4. Collapse phase of a bubble near PAA samples with different water content c for $\gamma \approx 0.88$. (*a*) $c = 95\%$, $\gamma = 0.92$; (*b*) $c = 85\%$, $\gamma = 0.88$; (*c*) $c = 70\%$, $\gamma = 0.9$; (*d*) $c = 60\%$, $\gamma = 0.88$ and (*e*) $c = 50\%$, $\gamma = 0.93$. Frame interval 1 μs; frame width 1.4 mm.

separates the upper and lower parts of the bubble and creates two axial jets flowing in opposite directions.

3.1.3. *Material dependence of the dynamics for* $\gamma \approx 0.4$

In the γ-range shown in figures 5 and 6 ($\gamma \approx 0.4$), a strong interaction between bubble and elastic boundary takes place and leads to erosion or ablation of the PAA sample over a large range of the elastic modulus. For the PAA sample with 95% water content and for $\gamma = 0.4$ (figure 5*a*), the bubble migrates away from the boundary during rebound and a liquid jet is developed which leads to the protrusion of the bubble wall farthest from the boundary. At $\gamma = 0.33$ (figure 6*a*), the jet propagates in the same direction, but bubble splitting occurs and a tiny cavity separates from the original bubble (frames 5–8). A surprisingly small elevation of the elastic boundary is visible in this photographic sequence, but the liquid appears cloudy near the PAA surface. Due to the high water content, the PAA sample is so soft that parts might be torn off and mixed with the water. This is not easily visible, however, because the refractive index of this PAA sample is very close to that of water.

Figures 5(*b*) and 6(*b*) show the case when the bubble is generated near the PAA sample with 85% water content. The main features of the bubble–boundary interaction are the formation of an annular flow leading to bubble splitting, a weak penetration of the liquid jet into the PAA sample (figure 5*b*, frames 15–17), and vortex shedding. The bubble collapses in an hour-glass shape with hardly any interaction with the ring vortex (figure 6*b*). The cap of the mushroom-shaped bubble collapses

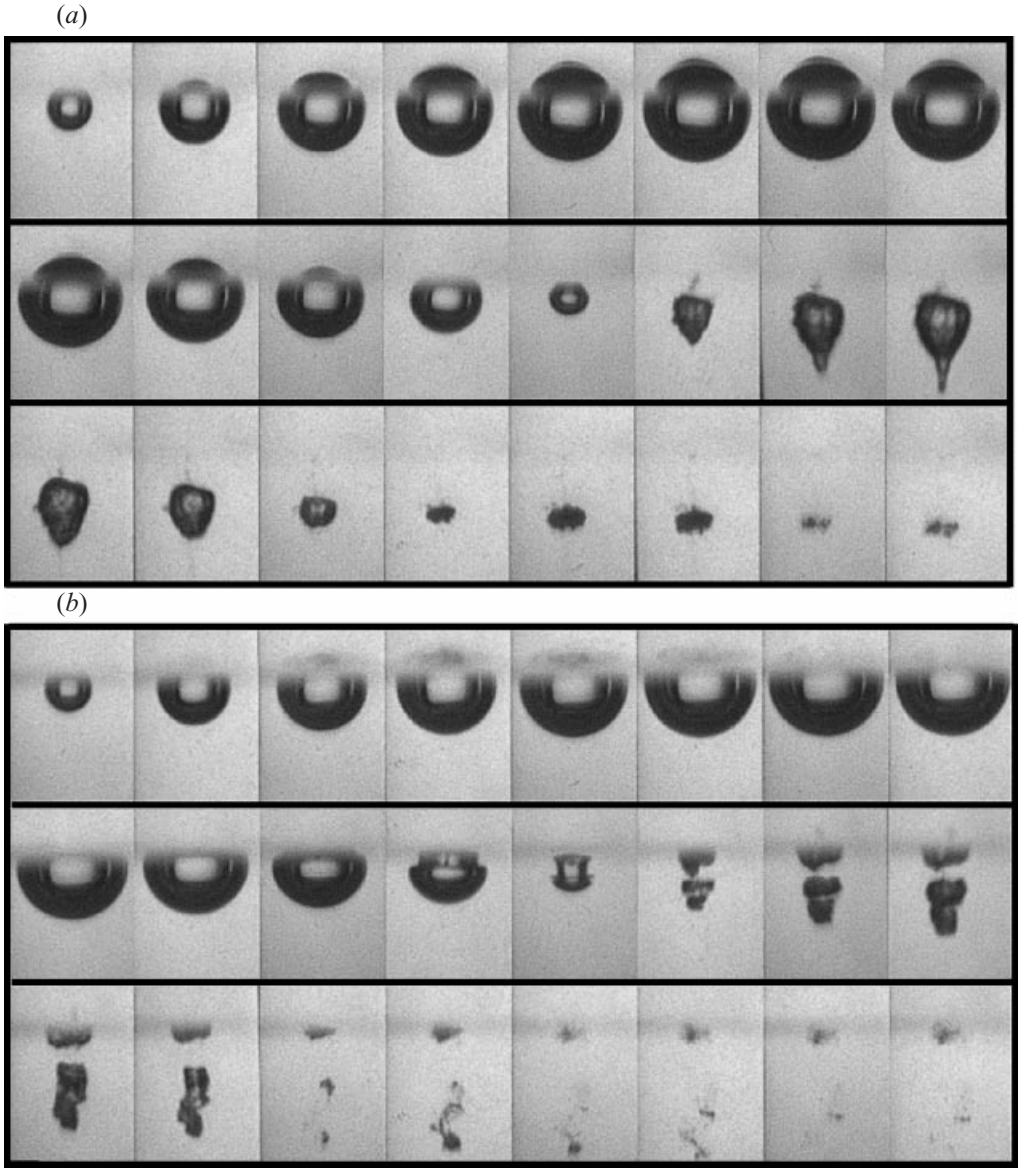

FIGURE 5 (*a,b*) For caption see facing page.

before the occurrence of the bubble splitting (figure 6*b*, frame 4) without emission of a strong shock wave. The liquid jet towards the elastic boundary is, therefore, only slightly stronger than the liquid jet in the opposite direction. A jet-like ejection of the PAA material into the surrounding liquid is visible in the series with 50 000 frames s^{-1} (figure 5*b*, frames 12 and 13), but not in the series taken with 1 million frames s^{-1} (figure 6*b*). As already described in Part 1, the PAA jet formation shows some irregularities near threshold. In the series without PAA jet formation, however, the PAA surface is strongly elevated during the last phase of the bubble collapse, and part of the rebounding cavity closer to the boundary seems to migrate into the PAA surface.

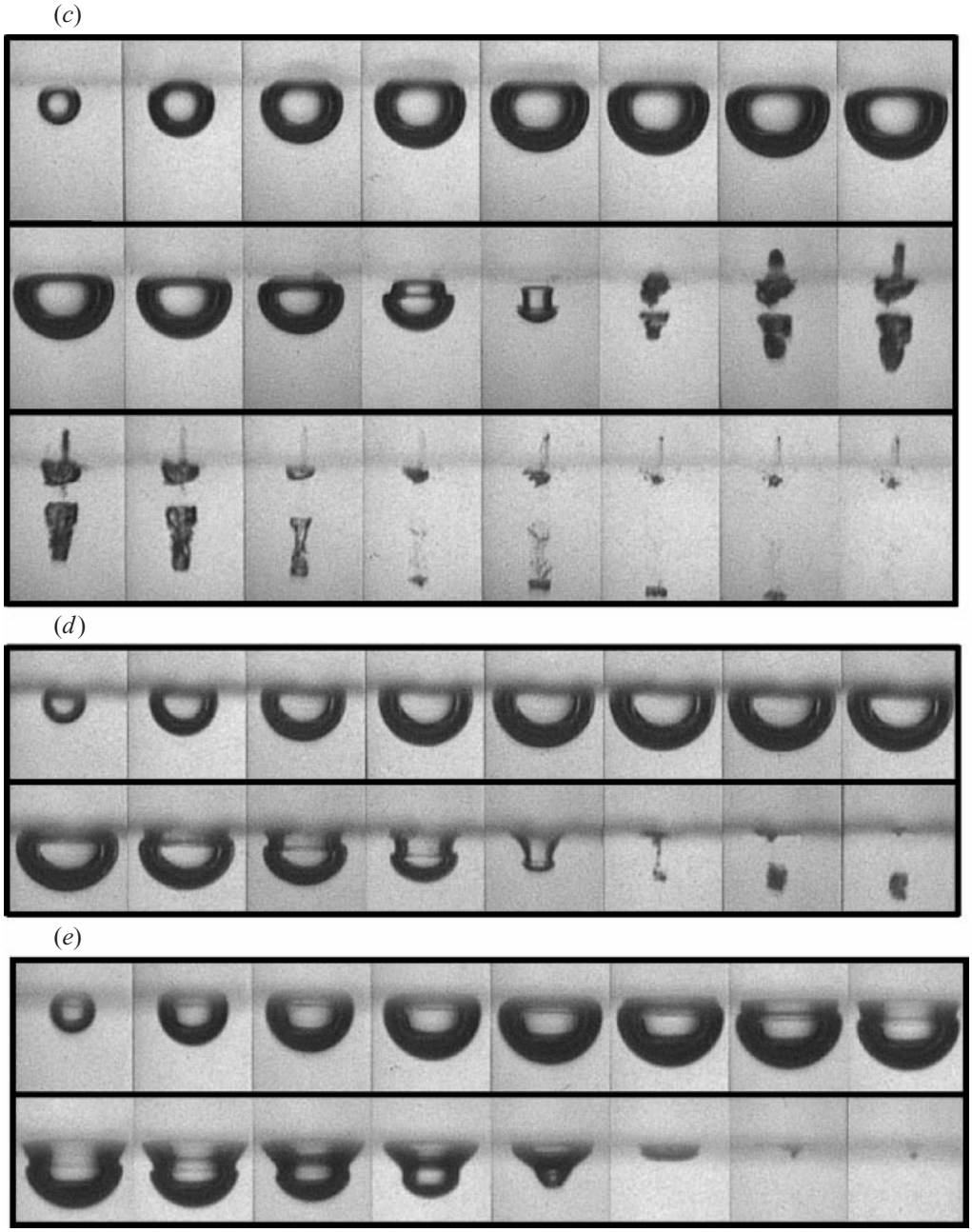

FIGURE 5. Growth and collapse of a laser-induced bubble near PAA samples with different water content c for $\gamma \approx 0.4$. (*a*) $c = 95\%$, $\gamma = 0.4$; (*b*) $c = 85\%$, $\gamma = 0.39$; (*c*) $c = 80\%$, $\gamma = 0.38$; (*d*) $c = 60\%$, $\gamma = 0.39$ and (*e*) $c = 50\%$, $\gamma = 0.4$. Frame interval 20 μs; frame width 3.5 mm.

The bubble dynamics near the PAA sample with 80% water content (figures 5*c* and 7*c*) is characterized by a strong annular jet flow resulting in two fast axial jets flowing in opposite directions. The formation of the PAA jet is again poorly reproducible around $\gamma = 0.4$, and no PAA jet is observed in the cases shown in figures 5(*c*) and 6(*c*). As a consequence, the liquid jet could penetrate deeply into the boundary. Figure

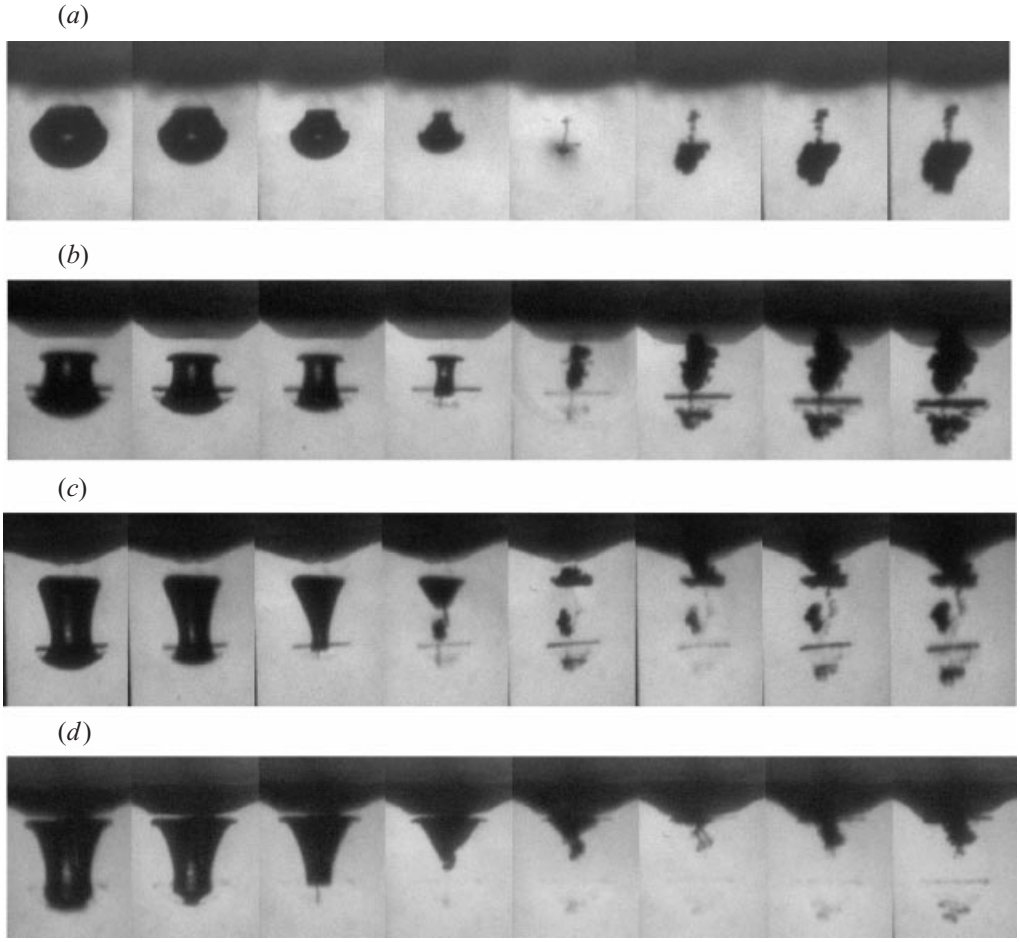

FIGURE 6 (*a,b*) For caption see facing page.

6 of Part 1 demonstrates, however, that the PAA jet formation may also occur in this parameter range. When the PAA jet is not developed, the measured value of the maximum velocity of the liquid jet directed towards the boundary is as large as $700\,\mathrm{m\,s^{-1}}$ ($\gamma = 0.43$, figure 6*c*).

For a water content of the PAA sample of 70%, a PAA jet develops and penetrates the bubble wall farthest from the boundary before the minimum bubble size is reached (figure 6*d*, frames 1 and 2). The jet becomes more clearly visible during the final collapse stage (figure 6*d*, frames 3–5). The PAA jet decelerates the liquid jet directed towards the boundary whose maximum velocity is, in this case, about $220\,\mathrm{m\,s^{-1}}$.

For PAA samples with 60% (figures 5*d* and 6*e*) and 50% water content (figures 5*e* and 6*f*), an annular flow is also developed, but it is asymmetric and results mainly in the formation of an axial liquid jet directed towards the boundary and in the shedding of a small cavity in the opposite direction. Again, because of the high material stiffness, no liquid jet penetration into the PAA sample occurs in spite of the large focusing angle of the jet flow and the small distance between bubble and boundary.

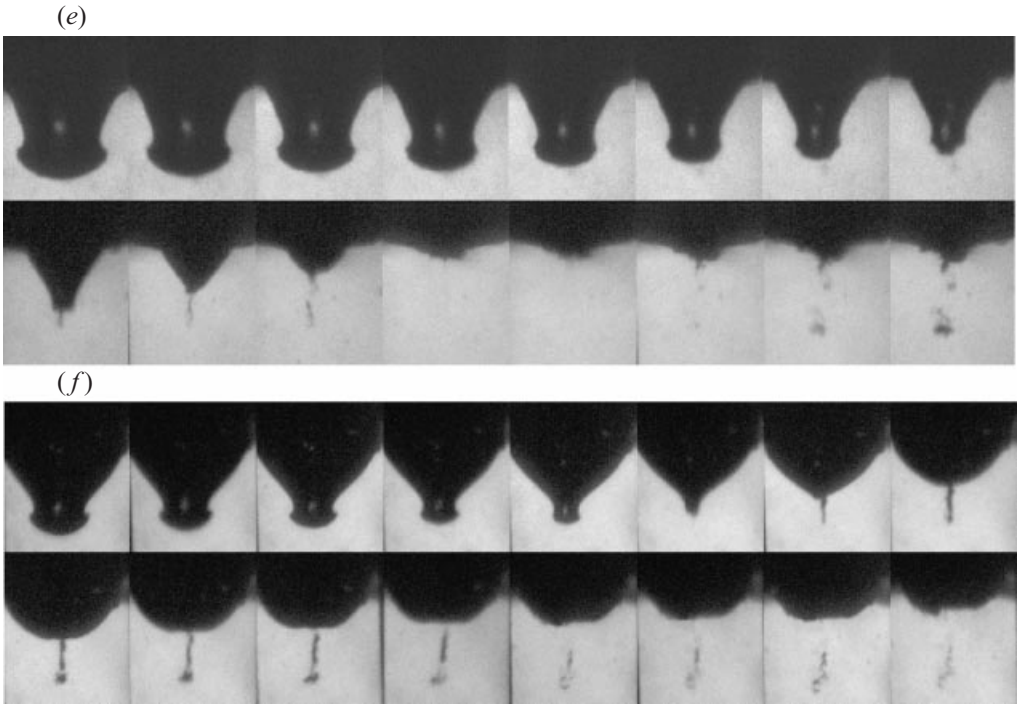

FIGURE 6. Collapse phase of a bubble near PAA samples with different water content c for $\gamma \approx 0.4$. (*a*) $c = 95\%$, $\gamma = 0.33$; (*b*) $c = 85\%$, $\gamma = 0.42$; (*c*) $c = 80\%$, $\gamma = 0.43$; (*d*) $c = 70\%$, $\gamma = 0.41$; (*e*) $c = 60\%$, $\gamma = 0.39$ and (*f*) $c = 50\%$, $\gamma = 0.52$. Frame interval 1 μs; frame width 1.4 mm.

3.1.4. *Material dependence of the dynamics for* $\gamma \approx 0.1$

Figures 7–9 show the dynamics for very small γ-values ($\gamma \approx 0.1$) which are of particular importance for cutting and ablation in medical laser surgery. When the bubble oscillates near the PAA sample with 95% water content, both jet formation and bubble migration are directed away from the boundary. The picture series taken with parallel illumination at 1 million frames s^{-1} demonstrate that the jet flow threading the bubble during the first (figure 8*a*) and second bubble collapse (figure 8*b*) consists of material from the soft PAA sample. As in figure 6(*a*), the refractive index of the PAA material differs only slightly from that of the surrounding water, but the jet concentrates material torn off from the PAA sample and is therefore better visible in these photographic series.

For samples of 85% water content (figure 7*b*), a PAA jet is ejected during the rebound of the deformed boundary surface which crosses the bubble (frames 7–11) and penetrates the opposite wall of the bubble (frame 12). During the bubble collapse, the surface of the PAA sample is strongly lifted and a volcano-like hump is formed. This, together with the PAA jet, is clearly visible in figure 9(*a*). After collapse, a part of the rebounding bubble migrates into the volcano-like hump (frames 5–8) which seems to have the form of a crater. At 80% water content (figure 9*b*), a PAA jet is also observed, but the deformation of the PAA surface induced by the bubble collapse is slightly weaker than that developed for 85% water content.

A moderate deformation of the boundary surface upon bubble collapse is also developed when the water content of the PAA sample is 70% (figures 7*c* and 9*c*), but no PAA jet is observed in this case. The bubble is repelled by the boundary during

(*a*)

(*b*)

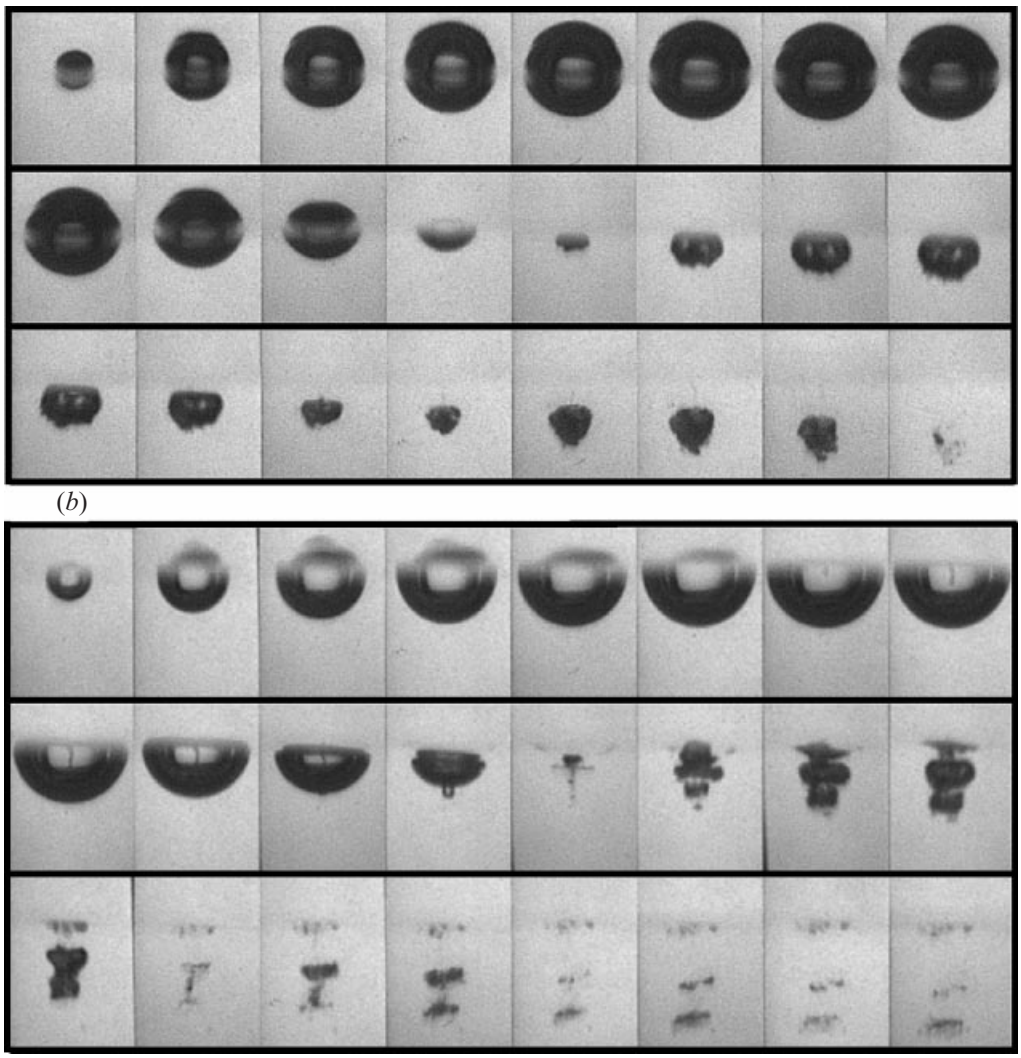

FIGURE 7 (*a,b*) For caption see facing page.

the very late stage of bubble collapse, and only a liquid jet directed away from the boundary is developed.

At 60% (figure not included) and 50% water content (figure 7*d*), the PAA sample is too stiff to allow a surface deformation which could lead to a jet-like ejection of PAA material into the liquid. The expanded bubble is approximately hemispherical, and an annular jet thus cannot develop. The bubble dynamics resembles that near a rigid boundary, with liquid jet formation towards the boundary (Vogel *et al.* 1989; Tomita, Shima & Takahashi 1991, Philipp & Lauterborn 1998). The liquid jet did not penetrate the PAA sample.

3.1.5. *Jetting behaviour as a function of E and γ*

Figure 10 gives a complete overview of the jetting behaviour as a function of the elastic modulus of the boundary E and the normalized bubble–boundary distance

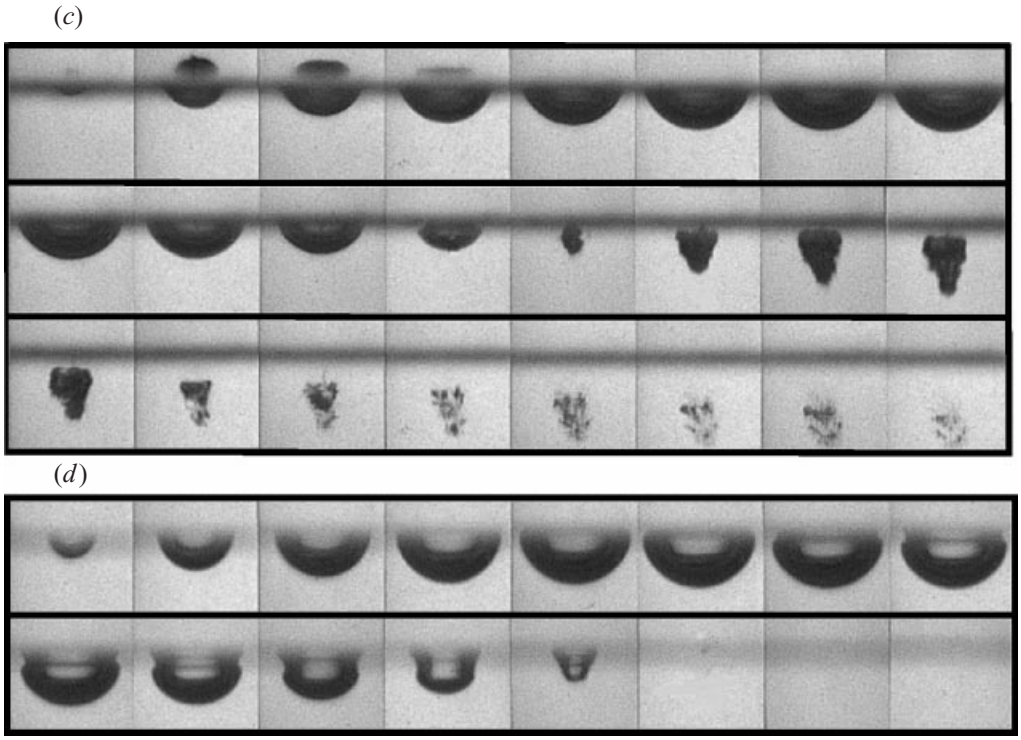

FIGURE 7. Growth and collapse of a laser-induced bubble near PAA samples with different water content c for $\gamma \approx 0.1$. (*a*) $c = 95\%$, $\gamma = 0.07$; (*b*) $c = 85\%$, $\gamma = 0.12$; (*c*) $c = 70\%$, $\gamma = 0.08$ and (*d*) $c = 50\%$, $\gamma = 0.08$. Frame interval 20 μs; frame width 3.5 mm.

γ. The range of elastic moduli investigated is centred around a region where the elastic response of the deformed boundary is particularly strong (0.12 MPa $< E <$ 0.4 MPa corresponding to a water content between 85% and 70%). With a larger elastic modulus ($E = 2.03$ MPa, corresponding to 50% water content), the bubble dynamics start to resemble the behaviour near a rigid boundary, whereas with a smaller elastic modulus ($E = 0.017$ MPa, at 95% water content), it becomes similar to the dynamics in an infinite liquid.

In a large region of the (E, γ)-parameter space, a jet flow directed away from the boundary develops – either as a unidirectional jet or as one component of a pair of jets flowing in opposite directions. This flow is a consequence of the elastic rebound of the boundary after its deformation during cavitation bubble expansion. At $E = 2.03$ MPa (50% water content), however, the PAA is already so stiff that the jet is directed towards the solid boundary like in the case of a rigid boundary.

The elastic response of the deformed boundary competes with the Bjerknes attractive force caused by the low pressure between bubble and boundary which develops during the collapse phase. At large γ-values and water concentrations $\leqslant 60\%$, the bubble dynamics is dominated by the elastic rebound of the boundary as can be deduced from the unidirectional jet flow away from the boundary. With decreasing γ-value, the attractive Bjerknes force increases faster than the strength of the flow from the boundary, and the magnitude of the opposing forces becomes more equal. This results in an oblate spheroidal shape of the expanded bubble which, in turn, leads to the formation of an annular jet and to subsequent bubble splitting with the

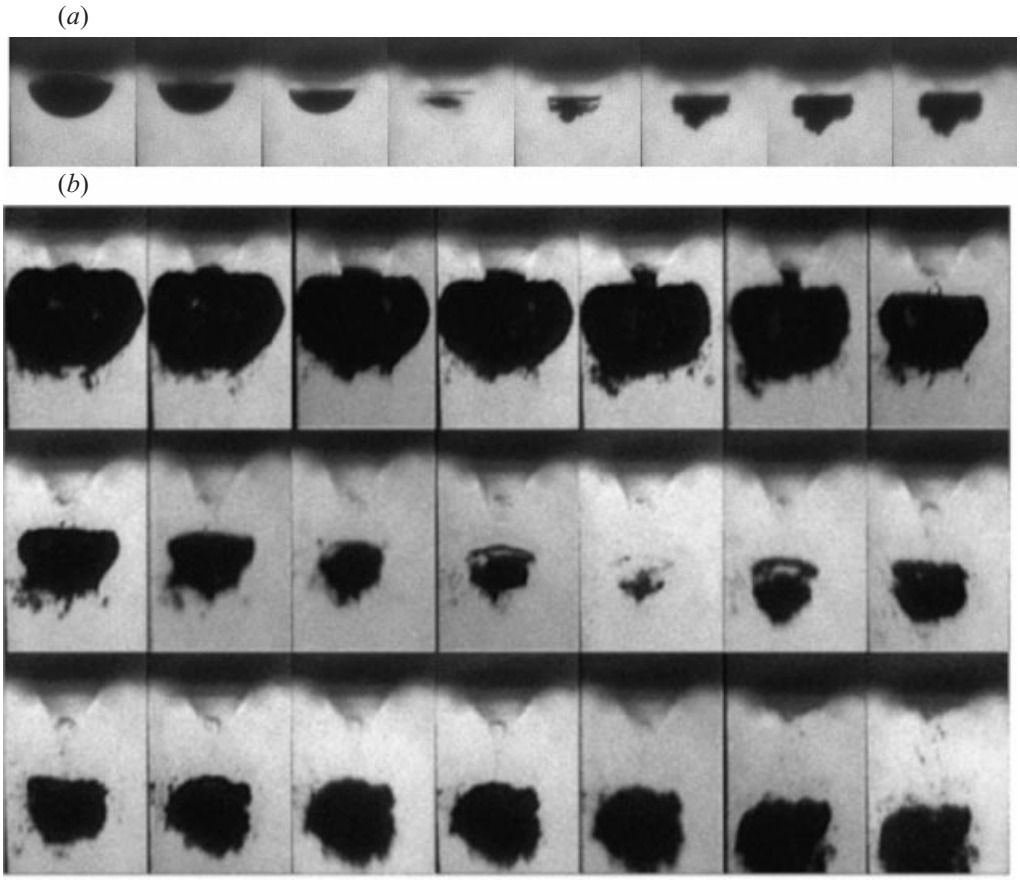

FIGURE 8. Collapse phase of a bubble near a PAA sample with 95% water content for $\gamma = 0.07$. (*a*) First collapse (frame interval 1 μs), and (*b*) second collapse (frame interval 5 μs). Frame width 1.4 mm.

formation of two axial liquid jets flowing in opposite directions (for a detailed analysis see Part 1). Bubble splitting occurs for γ-values smaller than about 1 together with values of the elastic modulus represented by 85% to 60% water content of the sample. For PAA samples with 95% and 50% water content, shedding of a tiny bubble from the main bubble is observed in a very small γ-range, but the bubble never splits into parts of approximately equal size. For very small γ-values, the bubble shape is most strongly curved near the surface of the PAA sample and the lateral flow is, therefore, strongest in this region. The bubble part closest to the boundary thus collapses first, the bubble migrates away from the boundary, and a liquid jet directed away from the boundary develops. A unidirectional liquid jet directed away from the boundary is, hence, formed both for very large and very small γ-values, but not in the intermediate γ-range.

A characteristic feature of the intermediate γ-range, i.e. the bubble splitting region, is the extremely high velocity of the axial jets formed at the end of the bubble collapse. A quantitative analysis of the jet velocities is given below in § 3.4. The high jet velocity results in a penetration of PAA samples with a water content between 70% and 85%. For smaller water concentrations, the PAA is too stiff to be eroded by a single liquid jet impact.

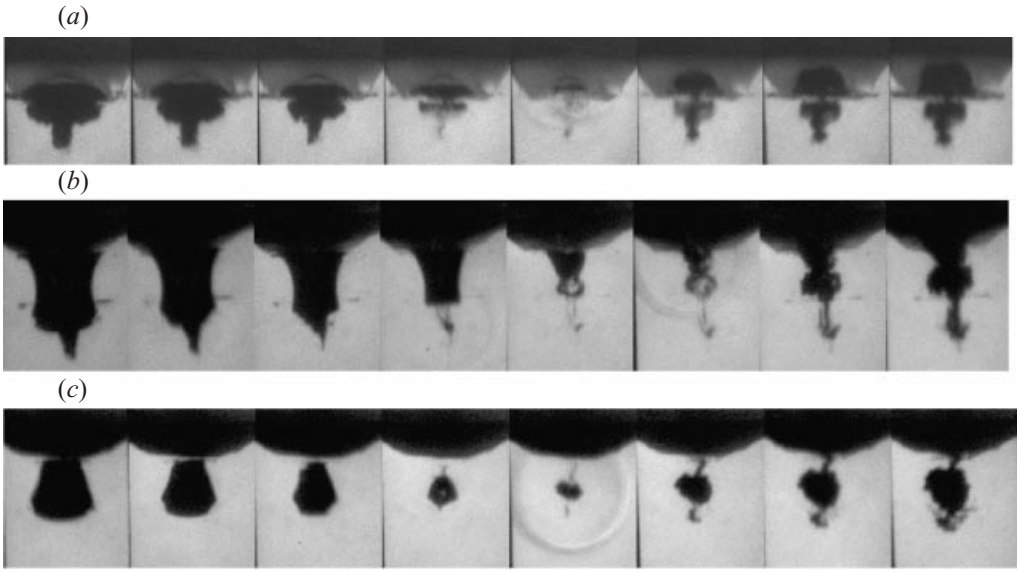

FIGURE 9. Collapse phase of a bubble near PAA samples with different water content c for $\gamma \approx 0.1$. (*a*) $c = 85\%$, $\gamma = 0.12$; (*b*) $c = 80\%$, $\gamma = 0.12$ and (*c*) $c = 70\%$, $\gamma = 0.08$. Frame interval 1 μs; frame width 1.4 mm.

Jet-like ejection of PAA material occurs for PAA samples with a water content between 70% and 85% and γ-values smaller than 0.6. At 60% and 50% water content, the elastic modulus is so large that the sample is only slightly deformed by the oscillating bubble.

3.2. *Bubble oscillation time*

Figure 11 shows the lengthening or shortening factor k against Rayleigh's oscillation time for all PAA samples investigated. For comparison, the values obtained for a flat rigid boundary (aluminium 99.9% purity, $E = 7.1 \times 10^4$ MPa) are also included. The interaction of the oscillating cavitation bubble with an elastic PAA boundary results in a shortening of the oscillation time compared with the case of a rigid boundary. The most pronounced reduction of the bubble oscillation time is observed for the PAA sample with 80% water content ($k < 1$). Because of its very pronounced elastic response, this material was chosen for the detailed investigations in Part 1. At larger values of the water content of the PAA sample, the bubble oscillation time approaches the limit of a spherical bubble in an infinite liquid ($k = 1$), while for smaller water contents, it is more similar to that obtained for a flat rigid boundary ($k > 1$). The elastic response of the PAA sample first leads to a shortening of the bubble expansion phase in the direction perpendicular to its surface and then to an acceleration of the bubble collapse in the same direction. Both factors contribute to the shortening of the oscillation time as well as to the creation of the oblate bubble shape which gives rise to the formation of an annular jet typical of the bubble dynamics near elastic boundaries.

3.3. *Bubble migration*

In regions of the parameter space where unidirectional jets are formed, the direction of the jet flow is the same as the direction of bubble migration during the collapse phase (Benjamin & Ellis 1966). The 'strength' of the bubble migration and jet formation can

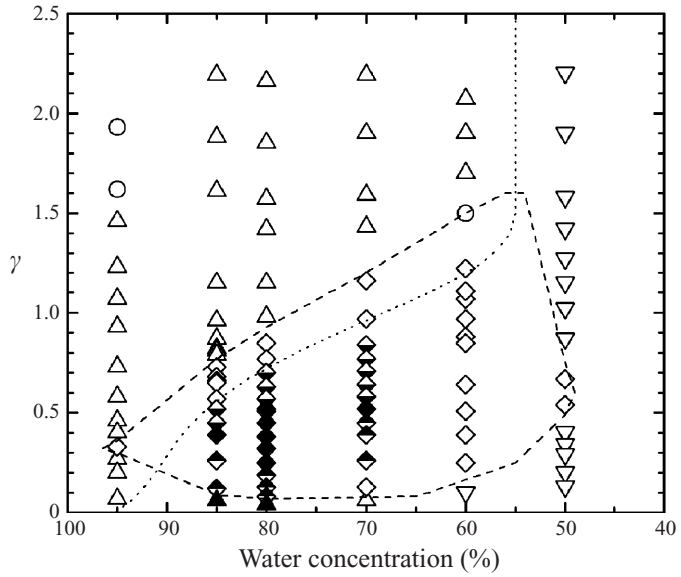

FIGURE 10. Jetting behaviour of laser-induced cavitation bubbles generated at various values of the dimensionless distance γ near elastic boundaries with different elastic modulus (PAA samples with different water contents): ○, no jet formation; △, liquid jet directed away from the boundary; ▽, liquid jet directed towards the boundary; ◇, liquid jets directed away from and towards the boundary; ⬙, liquid jets directed away from and towards the boundary, with liquid jet penetration into the PAA sample; ⬘, liquid jets directed away from and towards the boundary, and jet-like ejection of PAA material; ◆, liquid jets directed away and towards the boundary, with liquid jet penetration into the boundary and jet-like ejection of boundary material; ▲, liquid jet directed away from the boundary and jet-like ejection of boundary material into the liquid. The dashed line surrounds the bubble splitting region, and the dotted line denotes the state where the 'centre of gravity' of the two-bubble system does not migrate ('neutral bubble collapse').

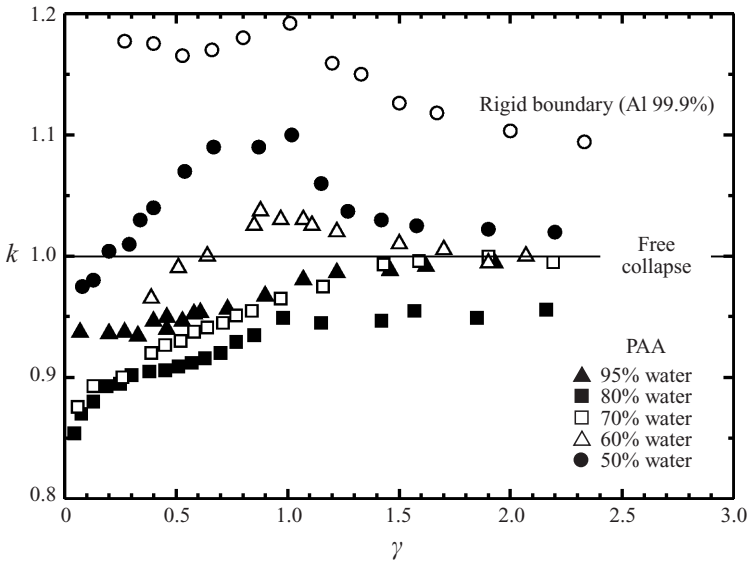

FIGURE 11. Values of the lengthening/shortening factor k of the oscillation period of a bubble generated near PAA samples of different water content, plotted as a function of the stand-off parameter γ. The respective data for an aluminum plate are included for comparison.

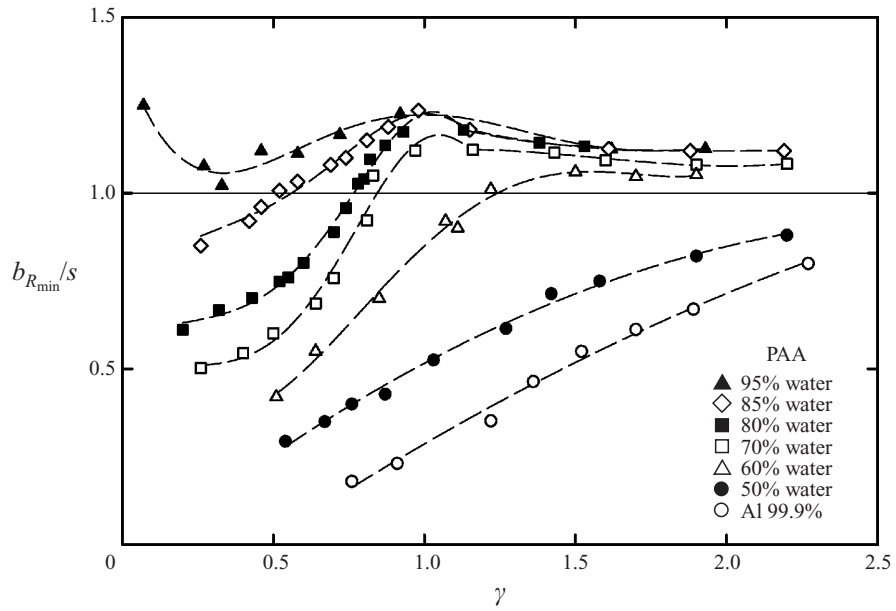

FIGURE 12. Migratory behaviour of a bubble oscillating near an elastic boundary. $b_{R_{\min}}$ is the distance between the bubble centre at its minimum size during first collapse and the boundary. For comparison the results obtained for a rigid boundary (aluminium plate) are also included.

be quantified by analysing the Kelvin impulse at the end of the bubble collapse (Blake *et al.* 1997). The Kelvin impulse describes the linear impulse of the bubble if one attributes a virtual mass to the bubble which corresponds to the liquid mass moving around the cavity. In the bubble splitting region, it is a measure of the difference in strength between the axial jets in opposite directions (see Part 1), and its calculation allows prediction of the migration of the centre of gravity of the two-bubble system (Blake *et al.* 1997).

The dotted line in figure 10 connects the (E,γ)-values with zero Kelvin impulse for which the 'centre of gravity' of the two-bubble system does not migrate. For larger γ-values and boundaries with a small elastic modulus, the bubble migrates away from the boundary, and for smaller γ-values or boundaries with a large elastic modulus, it moves towards the boundary. A quantitative evaluation of the bubble migration is shown in figure 12. The distance between bubble centre and boundary at first minimum bubble volume, $b_{R_{\min}}$, scaled by the initial distance between laser focus and boundary, s, is plotted as a function of the stand-off parameter γ. For $b_{R_{\min}}/s > 1$, the bubble migration is directed away from the boundary, while for $b_{R_{\min}}/s < 1$ the bubble is attracted by the boundary. The case $b_{R_{\min}}/s = 1$ corresponds to the neutral bubble collapse characterized by no bubble migration. It is obvious that the bubble migration depends not only on the stand-off parameter γ but also on the elastic properties of the boundary. With increasing stiffness of the sample, neutral bubble collapse occurs at ever larger γ-values, and the bubble migration approaches the results obtained for a rigid surface. It is worth noting that, when the bubble oscillates relatively close to an elastic boundary, it always migrates towards the boundary – except for the PAA sample with the smallest elastic modulus (95% water content), in which case the bubble migrates away from the boundary for all γ-values. Similar observations have been made by Shima *et al.* (1989) who investigated

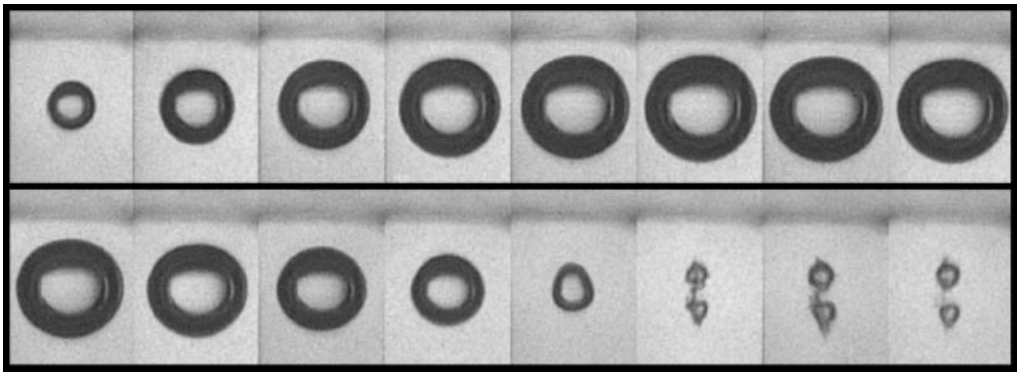

FIGURE 13. Bubble behaviour around the neutral collapse state. The bubble is generated near a PAA sample with 60% water content for $\gamma = 1.22$. Frame interval 20 μs; frame width 3.5 mm.

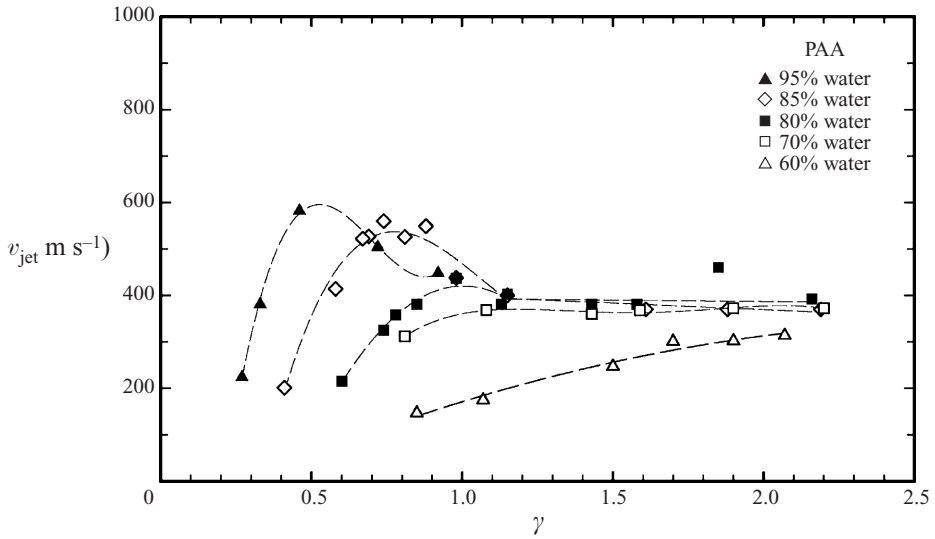

FIGURE 14. Maximum velocity of the liquid jet directed away from an elastic boundary.

the migratory characteristics of bubbles near a composite surface consisting of two layered viscoelastic materials.

It is interesting to note that the γ-values for zero Kelvin impulse (no migration of the centre of the two-bubble system) do not coincide with the γ-values where no jet formation occurs (circles in figure 10). This is particularly obvious for the sample with 60% water content. The case of no jet formation ($\gamma = 1.5$) is presented in figure 2(*c*), and figure 13 shows the case of zero Kelvin impulse ($\gamma = 1.22$) where the bubble splits in two nearly equal-sized cavities.

The data on bubble migration do not yield much information on the damage potential of the bubble–boundary interaction, because in the bubble splitting region, where the highest jet speeds are reached, they portray only the movement of the centre of the two-bubble system and do not allow an assessment of the velocities which can be reached by the individual liquid jets.

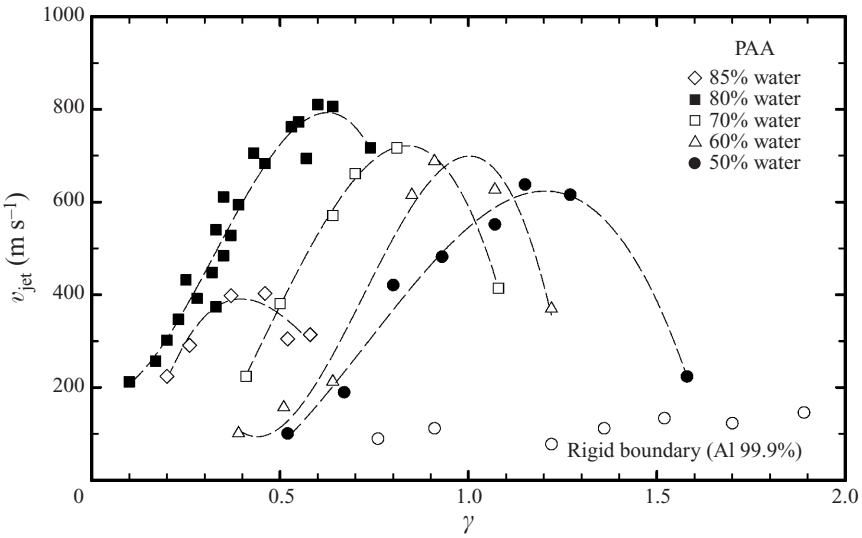

FIGURE 15. Maximum velocity of the liquid jet directed towards an elastic boundary.

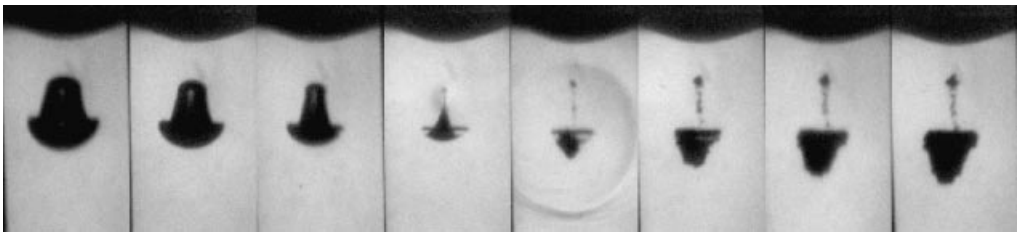

FIGURE 16. Illustration of the mechanism responsible for the generation of the ultra-high-velocity liquid jet directed away from an elastic boundary during the final stage of the bubble collapse. The bubble is generated near a PAA sample with 85% water content for $\gamma = 0.67$. Frame interval 1 μs; frame width 1.4 mm.

3.4. *Jet velocity*

The maximum jet velocities in the directions away from and towards the boundary were determined from the photographic series taken with 1 million frames s^{-1}, i.e. they represent the average velocity in a time interval of 1 μs. The results are plotted in figures 14 and 15, respectively. For comparison, the jet velocities measured near a flat rigid boundary (aluminium plate) are also included in figure 15.

For soft PAA samples (95% and 85% water content), the highest velocities (of about 550 m s^{-1}) are observed for liquid jets directed away from the boundary (figure 14). Figure 16 shows an example of jet formation away from a PAA sample with 85% water content where the maximum velocity is 560 m s^{-1}. It is obvious that the high-velocity jet emanates from the very high-curvature region of the cavity wall facing the boundary.

Near the stiffest PAA sample (50% water content), the liquid jet is directed towards the boundary and reaches a maximum velocity of about 600 m s^{-1} (figure 15). Even though the deformation of the boundary is not very pronounced, it is apparently strong enough to create an annular component of the jet flow which enlarges the solid angle from which the jet flow is focused and accelerates the jet to a final speed more than four times higher than near a rigid aluminium block (150 m s^{-1} at $\gamma = 1.89$).

In the bubble splitting domain (85% to 60% water content of the PAA sample),

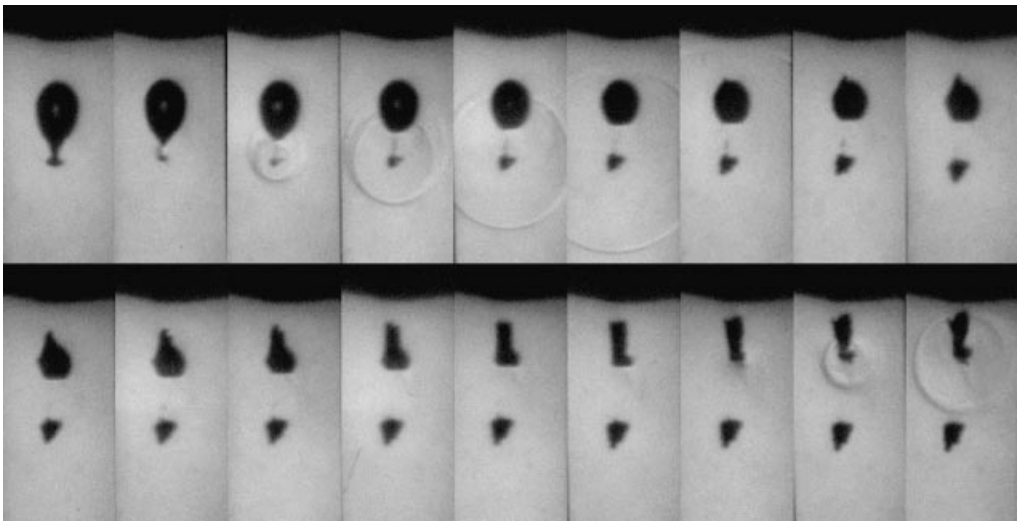

FIGURE 17. Illustration of the mechanisms responsible for the generation of the ultra high velocity jet directed towards an elastic boundary. The bubble is generated near a PAA sample with 60% water content for $\gamma = 0.91$. Frame interval 200 ns; frame width 1.4 mm.

fast jets are formed in both directions, but the highest velocities (up to 800 m s^{-1}) are measured in the direction towards the elastic boundary. These velocities are reached when an asymmetric annular jet focuses the fluid flow from a very large solid angle and the shock waves emitted upon the collapse of the bubble portion located away from the boundary hit the upstream wall of the cavity closer to the boundary. Figure 17 demonstrates the above considerations for the case of a bubble generated near a PAA sample with 60% water content when $\gamma = 0.91$. In this case, the maximum velocity of the liquid jet directed towards the boundary, averaged over 600 ns (between frames 4 and 7), is 720 m s^{-1}. In Part 1, we presented a case (80% water content, $\gamma = 0.6$) where the peak velocity averaged over 700 ns was as high as 960 m s^{-1}. The mechanism of jet formation was the same as presented here for the sample with 60% water content.

It is interesting to note that for the more compliant samples with smaller elastic modulus the maximum jet velocities are reached at smaller γ-values than for the stiffer samples. The reason is that compliant surfaces allow the formation of an oblate spheroidal bubble at smaller γ-values than stiff boundaries. As already mentioned, this bubble shape is essential for the development of an annular jet flow which is followed by the formation of fast axial jets.

The highest velocities of the liquid jet towards the boundary are reached near the PAA sample with 80% water content. The weaker elastic rebound of the PAA samples with lower water content (85% and 95%) causes a less pronounced flattening of the oblate spheroid and, therefore, a weaker annular jet. For example, the ratio of the long-to-short axes of the oblate spheroid at $\gamma \approx 0.4$ is 1.3 for a PAA sample with 80% water content, 1.22 for 85%, and only 1.12 for 95% water content. For stiffer samples, a more hemispherical shape is assumed by the expanded bubble. As a result, the liquid flow towards the boundary is, both for very soft and very stiff samples, not as strongly focused as that encountered when the bubble oscillates near the PAA sample with 80% water content, and the maximum velocities of the jets are therefore smaller.

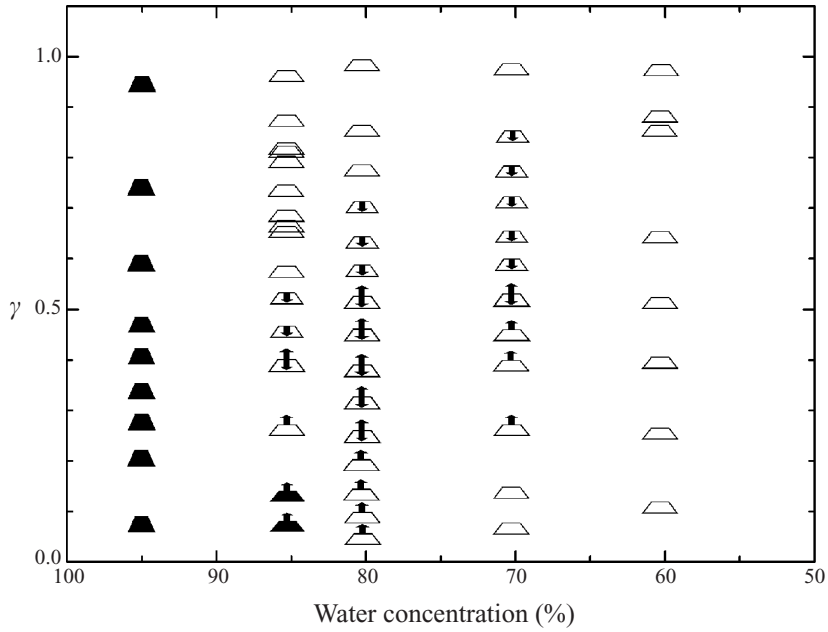

FIGURE 18. Mechanisms of cavitation erosion and cavitation-enhanced ablation of elastic materials and the regions in the (E, γ)-parameter space where they can occur. Trapezoid: uplifting of the boundary surface during bubble collapse (the filled symbols indicate that material is torn off from the PAA sample), arrow up: jet-like ejection of boundary material into the liquid, arrow down: liquid jet penetration into the boundary.

Ultra high-velocity jets emanating during the collapse of an oblate bubble near a flat rigid boundary have been theoretically predicted by Voinov & Voinov (1976). They found that the jet velocity increases with the bubble elongation, in agreement with the results of the present study. A jet velocity of 640 m s^{-1} was predicted for an initial bubble elongation of 17.5%.

4. Discussion

4.1. *Cavitation erosion and cavitation-enhanced ablation*

Three different mechanisms may contribute to cavitation erosion and to cavitation-enhanced ablation of elastic materials (see also Part 1): (i) liquid jet penetration into the material; (ii) formation of a jet consisting of elastic material directed into the surrounding liquid – this jet-like material ejection is a consequence of the elastic rebound of the deformed boundary; (iii) elevation and tearing of the material surface by the low pressure between bubble and boundary developing during bubble collapse. The regions for which these processes may occur are indicated in figure 18.

Liquid jet penetration into the material requires that the pressure generated by the impact of the liquid jet onto the boundary, is sufficiently high to overcome the yield strength of the material. For single laser exposures this is only the case for PAA samples with water contents between 70% and 85% at intermediate γ-values within the bubble splitting region. The most pronounced damage was observed when the bubble oscillates near the PAA sample with 80% water content. In this case, the sample is damaged over the largest γ-interval ($0.25 \leqslant \gamma \leqslant 0.68$) and the penetration

depth of the liquid jet is largest. For PAA samples with 50% and 60% water content, the yield strength is apparently too high to allow jet penetration.

We can obtain some information on the damage mechanism by comparing the jet impact pressure for those cases where the jet is just capable of penetrating the sample surface with the material strength of the PAA samples. The water hammer pressure of a jet with a flat tip is (Brunton 1966)

$$p_{WH} = \frac{\rho_1 c_1 \rho_2 c_2 v}{\rho_1 c_1 + \rho_2 c_2}, \tag{4.1}$$

where ρ_1, c_1 and ρ_2, c_2 are the respective densities and sound velocities in the jet and the impacted material, and v is the jet velocity. The impact pressure can be up to three times higher when the jet tip is round or conical (Lesser & Field 1983). As density and sound velocity in PAA (table 1) and water are very similar, (4.1) can be approximated by

$$p_{WH} = \tfrac{1}{2}\rho_1 c_1 v. \tag{4.2}$$

The duration of the water hammer pressure is given by the time required for the relaxation wave to travel from the periphery to the centre of the jet. It amounts to only 10 ns for a jet diameter of 30 μm. Afterwards, the PAA is affected by the dynamic pressure

$$p_{WH} = \tfrac{1}{2}\rho_1 v^2 \tag{4.3}$$

which lasts for several microseconds.

The impact velocity at the γ-values where the jet is just capable of penetrating a PAA sample with 80% water content ($\gamma = 0.25$ and $\gamma = 0.68$) is about $80\,\mathrm{m\,s^{-1}}$. That corresponds to a water hammer pressure of 60 MPa and a dynamic pressure $p_{\mathrm{dyn}} = 3.2$ MPa. At $\gamma = 0.74$, the impact velocity of the jet is only $10\,\mathrm{m\,s^{-1}}$, and no damage of the PAA material was observed (see figure 4 of Part 1). The jet velocity of $10\,\mathrm{m\,s^{-1}}$ corresponds to a water hammer pressure of 7.5 MPa and to a dynamic pressure of 0.05 MPa.

The data suggest that the threshold value of the water hammer pressure required to produce a macroscopically visible penetration of the PAA sample lies somewhere between 7.5 MPa and 60 MPa. This threshold value which represents an estimate of the dynamic yield strength of the PAA is considerably higher than the value of the compressive strength $Y = 0.54$ MPa which we obtained in measurements at a low strain rate of $\dot{\varepsilon} = 1.7 \times 10^{-3}\,\mathrm{s^{-1}}$ (see Part 1). The discrepancy can largely be explained by the fact that the strength of materials as well as their elastic modulus rise with increasing strain rate (Kolsky 1949). The strain rates involved in the impact of a jet with a velocity of $80\,\mathrm{m\,s^{-1}}$ are in the order of $\dot{\varepsilon} \approx 10^5\,\mathrm{s^{-1}}$. We could not measure E and Y at these high strain rates, because their determination requires elaborate dynamical testing procedures, such as the Hopkinson bar technique ($\dot{\varepsilon} \approx 10^3\,\mathrm{s^{-1}}$), Taylor impact ($\dot{\varepsilon} \approx 10^5\,\mathrm{s^{-1}}$), or plate impact ($\dot{\varepsilon} \approx 10^7\,\mathrm{s^{-1}}$) (Taylor 1946; Kolsky 1949; Nicholas & Rajendran 1990).

Besides the strain rate dependence of the yield strength, the short duration (10 ns) of the water hammer pressure may be another reason why a high value of the impact pressure is required to penetrate the PAA sample. A deep penetration of the PAA sample can probably only occur when both the water hammer pressure and the longer lasting dynamic pressure of the jet flow exceed the PAA material strength. This assumption is supported by the observation that the sample was not damaged when impacted by a jet with a velocity of $10\,\mathrm{m\,s^{-1}}$ which produces a dynamic pressure of only 0.05 MPa (1/10 of the PAA yield strength) – even though the water hammer

pressure at this jet velocity exceeds the yield strength measured at a low strain rate by a factor of 14. The sample was, on the other hand, penetrated by a jet with a speed of $80\,\mathrm{m\,s^{-1}}$ where p_{dyn} is 6 times larger than the compressive strength at low strain rate.

Jet-like ejection of the PAA has three prerequisites: (i) the PAA must be sufficiently deformed to allow geometric focusing effects during its rebound, (ii) the elastic modulus of the material must be sufficiently large so that the restoring force caused by the elastic deformation is large enough to cause this jet formation, (iii) the plastic flow stress of the material and the ultimate tensile strength of the material must be exceeded. These conditions are fulfilled for water concentrations between 70% and 85% and γ-values below $\gamma = 0.6$ (figure 18).

For a water content of the PAA samples of 70% to 95% and small to intermediate γ-values, the late stage of the bubble collapse is associated with a volcano-like uplifting of the boundary caused by the low-pressure region developing between the collapsing bubble and the boundary. The protrusion of the sample surface is much broader than the PAA jet, develops later, and is seen in a larger (E, γ)-parameter range than the PAA jet. For soft samples with 95% water content, the boundary is not only elevated by the low pressure between bubble and boundary, but the tensile strength of the PAA is exceeded and the liquid jet flow developing upon bubble collapse sucks in material from the PAA sample (figure 9). Some PAA material is also torn off during bubble collapse near samples with 85% water content (figure 10*a*). This mechanism of material erosion is due to the low pressure between the collapsing cavitation bubble and the PAA surface, and it must be clearly distinguished from the PAA ejection arising from the elastic rebound of the boundary itself. For samples with 85% water content this distinction is easy, because both processes occur sequentially. Both mechanisms contribute as well to the PAA material loss for samples with 95% water content, but here it is more difficult to identify their contributions. The restoring elastic force of the deformed material is too weak to produce a PAA jet into the liquid, but it is still strong enough to induce a bubble migration away from the boundary which allows a low pressure zone between bubble and boundary to develop that leads to the uplifting and tearing of the surface during the late collapse phase.

The dynamics described in this study for the interaction of cavitation bubbles with PAA samples is representative also of the interaction between laser-induced cavitation bubbles and biological tissues during medical laser surgery, because the range of elastic moduli investigated covers that found in soft tissues. Liquid jet penetration, the jet-like ejection of tissue or tissue debris into the surrounding liquid, and deformation by the tensile stress from the collapsing bubble may, therefore, all contribute to the ablation process in short-pulsed laser surgery. This is the case, for example, in laser thrombolysis (Godwin *et al.* 1998; Chapyak & Godwin 1998), and in orthopedic surgery (Grimbergen, Verdaasdonk & van Swol 1998). Frequently, however, these mechanisms are also the source of unwanted collateral effects limiting the local confinement of laser surgery, for example in intraocular tissue cutting near sensitive structures of the eye (Vogel *et al.* 1990; Vogel, Busch & Parlitz 1996; Vogel 1997).

4.2. *Comparison with previous results*

Most researchers have previously focused attention on the repulsion of bubbles by the elastic boundary which occurs preferentially at large γ-values, and applied the Kelvin impulse for the analysis of the migration of the bubble as a whole. This is useful in those regimes where single axial jets are formed, but the complex dynamics

in the bubble splitting region can only be fully understood by two-dimensional or three-dimensional analysis (see also Part 1).

Gibson (1968) worked with foam plastic of unknown elastic modulus, and Gibson & Blake (1980, 1982) worked with 1–6.8 mm thick rubber sheets. By contrast, in this study we have used homogeneous materials. In Gibson & Blake's studies, the rubber sheets were stretched across the base of a hollow cylinder, i.e. they acted like a drum. The drum-like setup implies that the elastic boundary is more easily deformable than a solid block with equal elastic modulus. The bubble dynamics observed by Gibson & Blake therefore resembles the dynamics observed in the present investigations for PAA samples with 95% water content, even though the elastic modulus of the rubber membranes (0.8–1 MPa) was about 50 times higher than that of the PAA samples (0.017 MPa). With the drum-like setup of Gibson & Blake, the response of the elastic material to the deformation can be modelled by a one-dimensional equation. This is not possible for the homogenous samples used in our study. Modelling here requires numerical simulations which would be beyond the scope of this paper.

Shima *et al.* (1989) worked with composite surfaces consisting of a layered structure of a Nitrile rubber sheet and a foam rubber backing. The test surface was lowered down onto a free water surface, so that the rubber sheet was surrounded by water, but the foam rubber backing remained outside. The composite surface possessed, hence, characteristics intermediate between a free surface and a rigid boundary. The composite wall stiffness and inertia were varied by varying the thickness of the rubber sheet. Their experiment was restricted to investigations of the migratory behaviour of the bubble and to large values of the stand-off parameter ($\gamma > 1$). When the thickness of the rubber sheet was increased, the same qualitative features of the bubble behaviour were found as described in the present study for an increase of the elastic modulus, namely a transition from bubble migration away from the boundary to bubble migration towards the boundary, with bubble splitting around the neutral collapse state. When, on the other hand, the boundary stiffness was decreased by reducing the thickness of the rubber sheet, the bubble behaviour became similar to that observed for a free surface because of the foam rubber backing of the rubber sheet. This case differs from the experimental conditions in the present study, where the bubble behaviour close to a soft, homogeneous PAA sample was investigated, which resembles the dynamics in a liquid of infinite extent.

Shaw *et al.* (1999) investigated the interaction of a laser-generated cavitation bubble with a flexible membrane of unknown elastic modulus for a dimensionless bubble–boundary distance of $\gamma = 0.8$. They observed the development of a mushroom-like bubble shape and bubble splitting, similar to the dynamics observed in the present study near PAA samples of 80% water content at equal γ. However, they were not able to conclusively explain their observations, because they considered only the inertia, but not the elastic response of the deformed membrane.

Recently, Kodama & Tomita (2000) have investigated the behaviour of laser-generated bubbles near gelatine samples with different water content for stand-off distances γ larger than 0.2. The elastic modulus of the gelatine samples was varied in the range 4.3×10^{-2} to 0.3 MPa which corresponds to that investigated here for PAA samples with a water content larger than 80%. They also observed the bubble splitting phenomenon and the uplifting of the boundary surface during bubble collapse but no observations were made concerning the formation of a liquid jet directed towards the boundary, liquid jet penetration into the elastic material and jet-like ejection of boundary material. For γ-values larger than 1.5, they reported similar results to those presented here with respect to both the migratory behaviour and the oscillation

period of the bubble. However, in contrast to the present results for $E > 0.1$ MPa they observed no shortening of the bubble oscillation period for $\gamma < 1.5$, and reported a continuous increase of the bubble migration away from the boundary with decreasing γ. Altogether, their results resemble our findings for PAA with 95% water content (corresponding to $E = 0.017$). The discrepancy may be due to different material properties of gelatine and PAA at high strain rates (the elastic modulus was in both studies measured only at low strain rates). The comparison of the results indicates that PAA reacts more stiffly at high strain rates than gelatine. Asshauer *et al.* (1997) showed that for PAA elasticity is dominant over viscous damping effects. It may well be that for gelatine the viscous damping is stronger than for PAA and the elastic response to laser-induced bubbles is, therefore, less pronounced. Another possible explanation for the discrepancy is that in Kodama and Tomita's experiment the sample was surrounded by a free surface rather than by a volume of liquid as in the present study.

Numerical calculations on the interaction of a bubble with a compliant elastic boundary were presented by Duncan and his co-workers (Duncan & Zhang 1991; Duncan, Milligan & Zhang 1996) who simulated the experiments by Shima *et al.* (1989). They achieved good agreement with the experimental results for bubble migration and neutral bubble collapse, but their investigations were, like the experiments, restricted to large values of the stand-off parameter ($\gamma > 1$). Duncan *et al.* (1996) predicted the fast movement of the boundary at the centre of its deformation which leads to an elevation of the boundary during bubble collapse. In the present investigations, this elevation was, in a fairly large parameter range, followed by a jet-like ejection of PAA material.

Cavitation-enhanced ablation has been reported recently by Chapyak & Godwin (1998) in the context of laser thrombolysis. They numerically simulated the interaction of a bubble with an elastic boundary for the specific case of $\gamma = 0$. The elastic modulus in their simulations was $E = 0.02$ MPa, and the plastic flow stress was 0.01 MPa. These values are similar to those of the PAA sample with 95% water content used in the present experiments. The calculations predicted a repulsion of the bubble by the elastic boundary, an elevation of the boundary upon bubble collapse and a jet-like material flow into the liquid during the final collapse stage, closely resembling the results of the present study.

5. Conclusions

The interaction of a laser-induced cavitation bubble with a homogeneous elastic material (PAA) was investigated by high-speed photography and acoustic measurements at values of the elastic modulus between $E = 0.017$ and $E = 2.03$ MPa and values of the dimensionless bubble boundary distance between $\gamma = 0$ and $\gamma = 2.2$. The interaction is very complex and depends strongly on E and γ. The response to the bubble dynamics also depends on the compressive and tensile strength of the material, but this dependence still needs to be investigated in detail.

(i) *Jetting behaviour*. In the range of 0.12 MPa $\leqslant E \leqslant$ 1.0 MPa, corresponding to 85%–60% water content of the PAA samples, the elastic response of the deformed boundary is particularly strong. The most prominent feature of the bubble dynamics at intermediate γ-values is the development of an annular jet leading to bubble splitting and to the formation of two very fast axial jets directed opposite to each other. In the parameter range $\gamma < 0.1$ and $\gamma > 1$, no bubble splitting occurs, and only an axial liquid jet directed away from the boundary is formed.

When the bubble oscillates near a boundary with large elastic modulus ($E = 2.03$ MPa, corresponding to 50% water content of the PAA sample), the liquid jet formed during the bubble collapse is always directed towards the boundary. For a boundary with small elastic modulus ($E < 0.02$ MPa, corresponding to 95% water content of the PAA sample), the liquid jet is always directed away from the boundary.

(ii) *Bubble oscillation time*. The interaction of the oscillating cavitation bubble with an elastic boundary results in a shortening of the oscillation time compared with the case of a rigid boundary. The most pronounced reduction of the bubble oscillation time below the Rayleigh collapse time in an infinite liquid is observed for the PAA sample with 80% water content ($E = 0.25$ MPa).

(iii) *Bubble migration*. In regions of the parameter space where unidirectional jets are formed, the direction of the bubble migration during the collapse phase is the same as the direction of the subsequent jet flow. In the bubble splitting region, the centre of the two-bubble system moves relatively slowly even though the migration of the individual bubble parts is fast and the velocities of the jets flowing in opposite directions are particularly high. When the original bubble splits into two parts of equal size, the centre of the two-bubble system remains stationary ('neutral bubble collapse').

(iv) *Jet velocity*. The fastest jet velocities are observed in the bubble splitting region when a slightly asymmetric annular jet focuses fluid from a large solid angle into an axial jet. This occurs at γ-values slightly smaller than those for neutral bubble collapse. The maximum velocity averaged over a time interval of 1 μs reaches $600\,\mathrm{m\,s^{-1}}$ for the jet directed away from the boundary and exceeds $800\,\mathrm{m\,s^{-1}}$ for the liquid jet flowing towards the boundary. That is much faster than the maximum jet velocity observed near a rigid aluminium boundary ($150\,\mathrm{m\,s^{-1}}$).

(v) *Cavitation erosion*. Cavitation erosion and cavitation-enhanced ablation of elastic materials may be caused by liquid jet penetration into the material, jet formation during rebound of the deformed surface which ejects material into the surrounding liquid, and rupture of the material surface by the low pressure developing during bubble collapse. For soft materials ($E = 0.017$ MPa, 95% water content of the PAA sample), only the last mechanism plays a significant role. For materials exhibiting a strong elastic deformation by the expanding cavitation bubble ($0.12 \leqslant E \leqslant 0.4$ MPa, 85% to 70% water content of the PAA sample), all three mechanisms come into play when γ is smaller than 0.6. For stiff materials ($E \geqslant 1$ MPa, 60% to 50% water content of the PAA sample), no macroscopic damage to the elastic boundary and no cavitation-induced ablation was observed after single laser shots. Liquid jet penetration deep into the PAA sample requires that the material strength is exceeded by both the water hammer pressure upon jet impact and the dynamic pressure of the jet flow.

We conclude that cavitation erosion cannot be prevented by covering rigid structures with elastic materials. On the contrary: in a fairly large region of the (E, γ) parameter space, erosion is even more pronounced than for rigid boundaries. In short-pulsed laser surgery, liquid jet penetration, the jet-like ejection of boundary material, and the tensile stress from the collapsing bubble can contribute to the desired ablation or cutting effect, but these processes may also cause unwanted collateral damage if fine effects merely consisting of tissue evaporation are desired.

Although our investigations shed new light on the intricate interaction of a bubble with an elastic boundary, the complex behaviour in the bubble splitting region is not yet fully explored. Numerical simulations of the bubble–boundary interaction could yield a valuable contribution to a better understanding of the complicated dynamics

by providing pressure contours and velocity vectors in the liquid surrounding the bubble which are not easily accessible through experiments.

Dr Brujan's stay at the Medical Laser Center Lübeck as well as a part of the computer facilities were sponsored by a grant of the Volkswagen Foundation (Grant Nr. 960.4-285). We thank Dr Wolfgang Köller of Medical University Lübeck for performing the measurements of the mechanical properties of the PAA sample, and appreciate valuable discussions on the bubble-induced deformation of the PAA surface with Dr Robert P. Godwin of Los Alamos National Laboratory.

REFERENCES

Asshauer, T., Delacretaz, G., Jansen, E. D., Welch, A. J. & Frenz, M. 1997 Pulsed holmium laser ablation of tissue phantoms: correlation between bubble formation and acoustic transients. *Appl. Phys.* B **65**, 647–657.

Benjamin, T. B. & Ellis, A. T. 1966 The collapse of cavitation bubbles and the pressures thereby produced against solid boundaries. *Phil. Trans. R. Soc. Lond.* A **260**, 221–240.

Blake, J. R., Hooton, M. C., Robinson, P. B. & Tong, R. P. 1997 Collapsing cavities, toroidal bubbles and jet impact. *Phil. Trans. R. Soc. Lond.* A **355**, 537–550.

Blake, J. R., Keen, G. S., Tong, R. P. & Wilson, M. 1999 Acoustic cavitation: the fluid dynamics of non-spherical bubbles. *Phil. Trans. R. Soc. Lond.* A **357**, 251–267.

Brujan, E. A., Nahen, K., Schmidt, P. & VOGEL, A. 2001 Dynamics of laser-induced cavitation bubbles near an elastic boundary. *J. Fluid Mech.* **433**, 251–281 (referred to herein as Part 1).

Brunton, J. H. 1966 High speed liquid impact. *Phil. Trans. R. Soc. Lond.* A **260**, 79–85.

Chapyak, E. J. & Godwin, R. P. 1998 Physical mechanisms of importance to laser thrombolysis. *Proc. SPIE* **3245**, 12–18.

Duck, F. A. 1990 *Physical Properties of Tissue*. Academic.

Duncan, J. H., Milligan, C. D. & Zhang, S. 1996 On the interaction between a bubble and a submerged compliant structure. *J. Sound Vib.* **197**, 17–44.

Duncan, J. H. & Zhang, S. 1991 On the interaction of a collapsing cavity and a compliant wall. *J. Fluid Mech.* **226**, 401–423.

Gibson, D. C. 1968 Cavitation adjacent to plane boundaries. In *Proc. 3rd Australasian Conf. on Hydraulics and Fluid Mechanics*, Sydney, pp. 210–214. The Institution of Engineers, Australia.

Gibson, D. C. & Blake, J. R. 1980 Growth and collapse of cavitation bubbles near flexible boundaries. In *Proc. 7th Australasian Conf. on Hydraulics and Fluid Mechanics*, Brisbane, pp. 283–286. The Institution of Engineers, Australia.

Gibson, D. C. & Blake, J. R. 1982 The growth and collapse of bubbles near deformable surfaces. *Appl. Sci. Res.* **38**, 215–224.

Godwin, R. P, Chapyak, E. J., Prahl, S. A. & Shangguan, H. 1998 Laser mass ablation efficiency measurements indicate bubble-driven dynamics dominates laser thrombolysis. *Proc. SPIE* **3245**, 2–11.

Grimbergen, M. C. M., Verdaasdonk, R. M. & Swol, C. F. P. van. 1998 Correlation of thermal and mechanical effects of the holmium laser for various clinical applications. *Proc. SPIE* **3254**, 69–79.

Hoeltzel, D. A., Altmann, P., Buzard, K. & Choe, K.-I. 1992 Strip extensiometry for comparison of the mechanical properties of bovine, rabbit, and human corneas. *Trans. ASME* E: *J. Biomech. Engng* **114**, 202–215.

Kodama, T. & Tomita, Y. 2000 Cavitation bubble behaviour and bubble-shock wave interaction near a gelatin surface as a study of in vivo bubble dynamics. *Appl. Phys.* B **70**, 139–149.

Kolsky, H. 1949 An investigation of the mechanical properties of materials at very high rates of loading. *Proc. Phys. Soc.* B **62**, 676–700.

Lesser, M. B. & Field, J. E. 1983 The impact of compressible liquids. *Ann. Rev. Fluid Mech.* **15**, 97–122.

Nicholas, T. & Rajendran, A. M. 1990 Material characterization at high strain rates. In *High Velocity Impact Dynamics* (ed. J. A. Zukas), pp. 127–296. John Wiley.

Phillip, A. & Lauterborn, W. 1998 Cavitation erosion by single laser-produced bubbles. *J. Fluid Mech.* **361**, 75–116.

Rayleigh, Lord 1917 On the pressure developed in a liquid during the collapse of a spherical cavity. *Phil. Mag.* **34**, 94–98.

Shaw, S. J., Jin, Y. H., Gentry, T. P. & Emmony, D. C. 1999 Experimental observations of the interaction of a laser generated cavitation bubble with a flexible membrane. *Phys. Fluids* **11**, 2437–2439.

Shima, A., Tomita, Y., Gibson, D. C. & Blake, J. R. 1989 The growth and collapse of cavitation bubbles near composite surfaces. *J. Fluid Mech.* **203**, 199–214.

Taylor, G. I. 1946 The testing of materials at high rates of loading. *J. Inst. Civil Engng* **26**, 486–518.

Tomita, Y., Shima, A. & Takahashi, H. 1991 The behaviour of a laser-produced bubble near a rigid wall with various configurations. In *Proc. ASME-JSME Fluid Engineering Conference*. FED vol. 116, pp. 19–25. ASME.

Vogel, A. 1997 Nonlinear absorption: intraocular microsurgery and laser lithotripsy. *Phys. Med. Biol.* **42**, 895–912.

Vogel, A., Busch, S. & Parlitz, U. 1996 Shock wave emission and cavitation bubble generation by picosecond and nanosecond optical breakdown in water. *J. Acoust. Soc. Am.* **100**, 148–165.

Vogel, A., Lauterborn, W. & Timm, R. 1989 Optical and acoustic measurements of the dynamics of laser-produced cavitation bubbles near a solid boundary. *J. Fluid Mech.* **206**, 299–338.

Vogel, A., Schweiger, P., Frieser, A., Asiyo, M. N. & Birngruber, R. 1990 Intraocular Nd:YAG Laser surgery: light tissue interaction, damage range, and reduction of collateral effects. *IEEE J. Quantum Electron.* **26**, 2240–2260.

Voinov, O. V. & Voinov, V. V. 1976 On the process of collapse of a cavitation bubble near a wall and the formation of accumulative jet. *Sov. Phys. Dokl.* **21**, 133–135.